***DNAJB1-PRKACA* fusion kinase drives tumorigenesis and interacts with β-catenin and the liver regenerative response.**

Authors
Edward R. Kastenhuber[1,2], Gadi Lalazar[3], Darjus F. Tschaharganeh[4], Shauna L. Houlihan[1], Timour Baslan[1], Chi-Chao Chen[1], David Requena[3], Sha Tian[1], Benedikt Bosbach[5], John E. Wilkinson[6], Sanford M. Simon[3], and Scott W. Lowe[1,7,8]

Affiliations

1. Department of Cancer Biology and Genetics, Memorial Sloan Kettering Cancer Center, New York, New York 10065, USA.
2. Louis V. Gerstner Jr. Graduate School of Biomedical Sciences, Memorial Sloan Kettering Cancer Center, New York, NY 10065.
3. Laboratory of Cellular Biophysics, The Rockefeller University, New York, NY 10065, USA.
4. DKFZ German Cancer Research Center, Heidelberg, Germany.
5. Oncology Target Discovery Program, Pfizer Inc., Pearl River, New York, USA.
6. Department of Pathology, University of Michigan School of Medicine, Ann Arbor, Michigan 48109, USA.
7. Howard Hughes Medical Institute, New York, New York 10065, USA.
8. To whom correspondence should be addressed. Email: lowes@mskcc.org.

Classification
BIOLOGICAL SCIENCES: Medical Sciences

Keywords
fibrolamellar hepatocellular carcinoma, liver cancer, mouse models, CRISPR, genome editing, protein kinase A, β-catenin

Abstract

A segmental deletion resulting in *DNAJB1-PRKACA* gene fusion is now recognized as the signature genetic event of fibrolamellar hepatocellular carcinoma (FL-HCC), a rare but lethal liver cancer that primarily affects adolescents and young adults. Here, we implement CRISPR/Cas9 genome editing and transposon-mediated somatic gene transfer to demonstrate that expression of both the endogenous fusion protein or a chimeric cDNA leads to the formation of indolent liver tumors in mice that closely resemble human FL-HCC. Notably, overexpression of the wild type PRKACA was unable to fully recapitulate the oncogenic activity of *DNAJB1-PRKACA*, implying that FL-HCC does not simply result from enhanced PRKACA expression. Tumorigenesis was significantly enhanced by genetic activation of β-catenin, an observation supported by evidence of recurrent Wnt pathway mutations in human FL-HCC, as well as treatment with hepatotoxin 3,5-diethoxycarbonyl-1,4-dihydrocollidine (DDC), which causes tissue injury, inflammation and fibrosis. Our study validates the *DNAJB1-PRKACA* fusion kinase as an oncogenic driver and candidate drug target for FL-HCC. Practical and scalable mouse models of this disease serve as a resource to further explore tumor development and treatment.

Significance

Limited resources are available for the treatment of FL-HCC and a lack of research tools have led to an absence of experimental characterization of the disease. Here, we describe a rapidly scalable method to generate synchronous cohorts of mice bearing FL-HCC tumors. We demonstrate that the *Dnajb1-Prkaca* gene fusion drives tumorigenesis in mice, and that fusion to DNAJB1 drives FL-HCC initiation more strongly than wild type PRKACA overexpression. The requirement of the PRKACA kinase domain reinforces the potential utility of kinase inhibitors targeting the fusion. By identifying genetic and environmental factors that can enhance the consistency and aggressiveness of disease progression, we reveal biological characteristics of the disease and advance a platform for future pre-clinical studies.

Introduction

FL-HCC ubiquitously harbors a ~400kb deletion on chromosome 19 that produces an in-frame fusion of the DnaJ heat shock protein family member B1 (*DNAJB1)* and protein kinase cAMP-activated catalytic subunit alpha (*PRKACA)* (**Fig. S1A**) (1, 2). *DNAJB1* encodes a subunit of the heat shock factor 40 (HSP40) complex, which activates the ATPase of HSP70 and serves as a molecular chaperone that can be induced by an array of environmental stresses (3). *PRKACA* encodes a catalytic subunit of protein kinase A (PKA), which resides in the cytoplasm in an inactive tetrameric complex with PKA C-β and two regulatory subunits of the PKA holoenzyme (4). Activation of GPCRs leads to cAMP-dependent dissociation of PKA regulatory and catalytic subunits and subsequent phosphorylation of a panoply of cellular substrates (4). The crystal structure of the DNAJB1-PRKACA fusion protein shows that the catalytic site, regulatory subunit binding and anchoring protein binding remain similar to the wild type PRKACA (5).

Beyond the presence of *DNAJB1-PRKACA* fusions, FL-HCC tumorigenesis is poorly understood. Few, if any, other significantly recurrent mutated genes have been described (6, 7). While copy number alterations have been observed, they do not directly implicate any additional known oncogenes or tumor suppressors (7). Also, unlike liver cancer in older adults, FL-HCC is not associated with any known etiological risk factors such as alcoholism, chronic hepatitis infection, or liver flukes (8).

Currently, FL-HCC is diagnosed histologically, described as large cells with granular eosinophilic cytoplasm, vesiculated nuclei, and large nucleoli. Ultrastructural studies observe a hyperaccumulation of mitochondria and abundant endoplasmic reticulum (9). While young age and lack of chronic liver disease are suggestive of FL-HCC, classic HCC can also occur in young patients and misdiagnosis is common (10). Based on the biological sensitivity and specificity of the presence the *DNAJB1-PRKACA* fusion, its detection will likely become considered critical for diagnosis of FL-HCC (2).

Surgical resection is currently the primary treatment for FL-HCC patients. Although often described as a relatively indolent disease, a high rate of recurrence represents a major clinical challenge (11) and the 5-year survival rate is 34% (12). There is no evidence of survival benefit from adjuvant chemotherapy or any systemic treatment applicable to classic HCC (13). The unique demographics and genetics of FL-HCC suggest that these patients should be treated differently than those harboring HCC,

but since the disease is rare there have been few clinical trials (www.clinicaltrials.gov). Advancements in improving patient outcomes are hindered by the lack of good experimental systems to study the biology and treatment of FL-HCC biology beyond clinical correlations.

Mouse models have been a powerful tool to evaluate the oncogenic potential of candidate drivers, to study the biology of tumorigenesis, and as preclinical systems to test novel therapeutics (14). We employed hydrodynamic transfection combined with either CRISPR/Cas9-mediated editing of the endogenous deletion or transposon mediated transgenesis of fusion cDNA and variants, allowing us to introduce genetic lesions in a subset of hepatocytes without the time and expense of producing germline genetic strains (15, 16). Using this approach, we demonstrate that the *DNAJB1-PRKACA* fusion is a bona-fide oncogene and identify genetic and environmental factors that cooperate with this genetic event to drive aggressive disease. Our results further show that the kinase domain of PKA is required for these effects, providing rationale for targeting kinase activity pharmacologically. We anticipate that the models presented herein will serve as a powerful platform for future biological and pre-clinical studies.

Results

CRISPR-mediated deletion results in fusion oncogene and drives tumorigenesis in vivo.

The oncogenic potential of the endogenous *DNAJB1-PRKACA* fusion *in vivo* was assessed. Co-expression of Cas9 with multiple sgRNAs can be used to model chromosome translocations, inversions, and deletions by generating DNA double strand breaks (DSBs) at the breakpoints of chromosome rearrangements, which are subsequently joined by non-homologous end-joining (NHEJ) (17-21). While such events are rare, if the resulting rearrangement is oncogenic, it is positively selected *in vivo*. We reasoned that the FL-HCC-associated rearrangement could be generated in the livers of young adult mice via hydrodynamic tail vein injection of tandem guide CRISPR constructs targeting the first introns of *Dnajb1* and *Prkaca*, corresponding to the breakpoints of the disease-associated deletion (**Fig. 1A**). Importantly, the deleted region on human chromosome 19 in FL-HCC is syntenic to a corresponding region on mouse chromosome 8. In fact, all protein-coding genes present in the human region have orthologs present in the mouse region, and are arranged in the same order (**Fig. 1A**).

Cas9 linked to sgRNAs capable of targeting the first intron of Dnabj1 and Prkaca were introduced into NIH3T3 cells or adult livers using lentivirus transduction or hydrodynamic injection, respectively (Fig. S1A) and the intact fusion was detected by PCR (**Fig. S1B, C**). Cohorts of mice were injected with vectors containing two independent sgRNA pairs targeting different sequences within the same introns (herein CRISPR.1 and CRISPR.2). A subset of animals became moribund with liver tumors 16-24 months post injection (**Fig. 1B**). Tumor-bearing mice typically harbored disease involving multiple lobes, presumably from independent initiating events and ranged from diffuse to macroscopically visible (**Fig. 1C**). In total, 3/10 mice injected with CRISPR.1, and 3/8 mice injected with CRISPR.2, died as a result of tumor burden. Non-moribund animals that were sacrificed harbored histological evidence of disease (annotated as "asymptomatic") in 2/10 CRISPR.1 mice and 2/5 of CRISPR.2 mice (**Fig. 1D**). For both guide pairs, RT-PCR and Sanger sequencing with fusion-specific primers confirmed expression of the intended Dnajb1-Prkaca fusion oncogene in these lesions (**Fig. 1E**).

The morphology of CRISPR-induced mouse tumor cells (**Fig. 1F**) is strikingly similar to human FL-HCC histopathological presentation (**Fig. 1G**). Mouse liver lesions, like human FL-HCC, are composed of large, pleiomorphic polygonal cells with abundant eosinophilic cytoplasm, large vesicular nuclei and prominent nucleoli. Other features of human FL-HCC include cytoplasmic inclusions, mitotic figures and choleostasis (see below). Unlike the human disease, fibrosis was not present in the model. Lobular structure is clearly disrupted in mouse FL-HCC, as compared to normal liver, where sinusoids connect central veins to portal triads (**Fig. 1H**). In an independent experiment, tumors with similar latency and histology were recapitulated with an independent vector expressing Cas9 from an EF1a promoter (**Fig. S1D**). Thus, induction of an endogenous *Dnabj1-Prkaca* fusion through intrachromosomal deletion drives tumors with features of FLHCC in mice. Independent work from others recently demonstrated an FL-HCC phenotype of early lesions in asymptomatic mice using similar methods (22).

DNAJB1-PRKACA chimera drives liver tumorigenesis.

The segmental deletion that results in the *DNAJB1-PRKACA* gene fusion entails heterozygous loss of 7 other coding genes, with unknown functional contribution. In other contexts, such deletions can contribute to tumorigenesis directly through attenuating the function of haploinsufficient tumor suppressors (23). To determine whether the DNAJB1-PRKACA fusion is sufficient to drive tumorigenesis and, if so, whether the simple overexpression of the wild-type PRKACA gene could recapitulate this effect, we used hydrodynamic injection to deliver a transposon expressing the human *DNAJB1-PRKACA* fusion cDNA or a full length wild-type *PRKACA* cDNA. Co-transfection of sleeping beauty transposase ("SBase") with a transposon construct allows for stable integration and constitutive expression of the cDNA in the absence of insertional mutagenesis following clearance of the non-integrating transposase, permitting sustained overexpression of the fusion protein that mimics the high levels in human tumors (1) (**Fig. 2A**).

Although expression and protein stability are similar between the DNAJB1-PRKACA fusion protein and full-length WT PRKACA, and overexpression of wild type PRKACA was produced some changes to hepatocyte histology, it did not trigger the formation of lethal tumors (**Fig. 2B-D**). However, following delivery of the *DNAJB1-PRKACA* cDNA, we observed tumors with similar kinetics, penetrance, and morphology as CRISPR-driven murine FL-HCC (**Fig. 2B,C,E**). Again, a spectrum of histological findings supported the similarity between these lesions and human FL-HCC (**Fig. 1,2**), including the presence of large, often multi-nucleated, tumor cells with granular, eosinophilic cytoplasm and prominent nucleoli (**Fig. 2F**). Cholestasis and distinctive cytoplasmic inclusions (pale bodies) were also seen (**Fig. 2F**). Pale bodies and hyaline bodies are each present in about half of human FL-HCC cases (8). These results imply that the DNAJB1 portion of the fusion contributes to disease beyond facilitating overexpression of PRKACA that the chromosome 19 deletion event is dispensable for oncogenesis.

Histological and structural features of murine FL-HCC.

To explore which disease-associated phenotypes can be directly attributed to the *DNAJB1-PRKACA* fusion in greater detail, we performed additional histological characterization of murine FL-HCC tumors. Ultrastructural analysis by electron microscopy (EM) revealed numerous features of FL-HCC. With respect to adjacent normal hepatocytes, which were often compressed at the tumor margins, tumor cells were enlarged with clumped heterochromatin (**Fig. 3A-D, S2A**). Reminiscent of an FL-HCC-specific phenotype identified in previous studies of the human disease (8, 9, 24), murine FL-HCC tumor cells contain strikingly high numbers of mitochondria with atypical appearance and abundant endoplasmic reticulum (yellow arrows, **Fig. 3B,E,F, S2E-H**). The mitochondria were round to oval and homogeneous without obvious cristae and numerous megamitochrondria were observed. Mitochondria were surrounded by a rich accumulation of rough endoplasmic reticulum (red arrows, **Fig. 3E-F,S2**), but little smooth endoplasmic reticulum.

The cell-of-origin of FL-HCC remains unidentified, but human cases have been described to express mixed lineage markers (25, 26). The mouse tumors appear to stain positive for hepatocyte markers HNF4A and HNF1A, with some tumor cells showing reduced expression, consistent with reduced hepatocyte lineage commitment (**Fig. S3A,B**). The tumor cells are negative for biliary markers CK7 and CK19 and negative for CD68 (**Fig. S3C-F**).

Unexpected observations including occasional necrotic cells and abnormal tumor-associated vessels were seen (**Fig. 3B**). Throughout the tumor, cells had moderate to severe perinuclear aggregates of lipofuscin, a stress-related pigment that was also seen in the cytoplasm (**Fig. 3D,E**). Tumor cell-cell margins were indistinct and cell-cell junctions were either simple or not obvious (**Fig. S2A,B**), potentially indicative of decreased cell adhesion. As additional evidence of decreased cell-cell adhesion, membranous E-cadherin expression was reduced (**Fig. 3G**). There is also a remarkable loss of cell polarity, indicated by a loss of synchronized glycogen storage amongst neighboring hepatocytes (**Fig. 3G**). Elevated membranous β-catenin was seen, as was known PKA phosphorylation site (27) phospho-β-catenin^{S675} (**Fig. 3G, Fig. S7**). However, nuclear β-catenin staining was not appreciable in tumor samples.

<u>Transcriptional profiling of murine FL-HCC confirms similarities to the human disease and suggests processes linked to tumorigeneis.</u>

Murine FL-HCC tumors and control liver tissue were transcriptionally profiled by RNA-Seq (**Supplementary Table 1**). Reads that cross the junction were observed, confirming expression of the fusion (**Fig. 4A**). Principal component analysis demonstrated that the vast majority of the variance described the differences between tumor and normal samples (**Fig. 4B**). A total of 5710 genes were significantly differentially expressed between tumor and normal tissue (**Supplementary Table 2**). A focused analysis to investigate the similarity between mouse and human tumors was evaluated in two ways. First, single sample gene set enrichment analysis (ssGSEA) (28) using FL-HCC expression signatures from three independent published studies (7, 10, 29) was used to confirm that genes differentially expressed in human tumors were, in aggregate, significantly enriched in our murine tumors (**Fig. 4C**). Second, a supervised analysis of curated functional gene sets previously reported as enriched in FL-HCC (29) were consistent with murine tumor expression data (**Fig. S4A**). These results provide an unbiased analysis that classifies the murine model as FL-HCC.

This analysis also identified other biological and molecular features that are consistent with previous observations in human tumors. Global analysis of differentially expressed genes using GSEA revealed expression patterns suggesting biological processes associated with transformation (**Fig. 4D,E, Supplementary Table 3**). For example, cell cycle and DNA biosynthesis gene sets, and specifically *Cdk1*, *Gins2*, and *Cenpa,* were highly upregulated in the experimental tumors (**Fig. 4D,E**), which also showed alterations in mitogenic signaling genes such as downregulation of *Deptor* (a negative regulator of mTORC1 also decreased in human tumors), as well as upregulation of the RTK ligands *Egf*, *Nrg2*, and *Ereg* was observed in murine tumors (29) (**Fig. S4E**). Supporting the notion that dedifferentiation is a feature of *DNAJB1-PRKACA* driven transformation, we observed downregulation of hepatocyte lineage markers and upregulation of some neuroendocrine markers (**Fig. 4D, S4G**), as has been observed in human FL-HCC (29). GSEA further showed downregulation of epithelial cell fate commitment, bile acid biosynthesis, liver specific genes, and xenobiotic metabolism and upregulation of a teratoma-associated gene set (**Fig. 4E**). Similarly, hepatocyte gene expression is linked to distinct specialized zones (30), were universally lost, further supporting a role for the loss of cell lineage identity in FL-HCC development (**Fig. S4H**).

Our analysis also suggested yet other biological processes that may be relevant to FL-HCC pathogenesis that have not been previously appreciated. *Cdh1*/E-cadherin as well as cell adhesion and desmosomes gene sets were downregulated, reinforcing histological and ultrastructural findings consistent with decreased cell-cell adhesion in murine FL-HCC (**Fig. 4D,E**). Lastly, reaction to oxidative stress is indicated by the upregulation of enzymes involved in detoxifying reactive oxygen species (e.g. *Nqo1*, *Gpx3*, *Gpx4, and Acox1*) (**Fig. 4D,S4F**). The accumulation of mitochondria can be driven by oxidative stress (32), and interestingly, all detected transcripts encoded by the mitochondrial genome trended towards mild upregulation, consistent with hyperaccumulation of mitochondria seen by EM (**Fig. S4B**). Oxidative stress may also be related to the induction of inflammasome-associated genes (**Fig. 4E**) and the accumulation of lipofuscin (**Fig. 3F**) (33, 34), potentially helping to reconcile the elevated cell cycle rate with the indolent phenotype and growth rate of the tumors. It is possible that the kinetics of the tumors might indicate the requirement of secondary spontaneous genetic alterations for tumorigenesis, but copy number profiling by low-pass whole genome sequencing of a murine FL-HCC shows at least no significant genomic amplifications or deletions (**Fig. S4A**).

<u>WNT pathway cooperates with fusion to accelerate FL-HCC tumorigenesis</u>

To further understand FL-HCC tumorigenesis, and to address the long latency of the single hit models, we investigated additional factors that could accelerate disease. We queried the MSK-IMPACT collection of clinical sequencing data, which contains targeted sequencing data of over 18,000 cancer patients (35). Eighteen liver cancer patients (age 18-36) whose tumors harbored the *DNAJB1-PRKACA* fusion were identified (**Fig. 5A**). As expected, the fusion was not detected in any liver cancer patient over the age of 36 (0/414 patients) or in any non-liver cancer patient (0/18,367 patients), confirming the remarkable specificity of the *DNAJB1-PRKACA* fusion to liver oncogenesis (**Fig. S6A**). While HCC and intrahepatic cholangiocarcinoma (ICC) share several mutations among the most commonly mutated genes of each disease, none of these have been previously described in FL-HCC. Surprisingly, we noted previously unreported recurrent mutations in the Wnt pathway in human FL-HCC (**Fig. 5A,B**). The MSK-

IMPACT cohort contains 3/18 (17%) cases of FL-HCC with *CTNNB1* or *APC* mutation (age 18-21 years old).

In parallel, candidate drivers of liver cancer were evaluated for their ability to synergize with *DNAJB1-PRKACA* to transform hepatocytes. Neither transposon based delivery of *MYC*, *AKT*^{myr}, *NOTCH*^{ICD}, *YAP*^{S127A}, *Fgf15*, *Il10*, *Il18*, *Tgfb1*, nor Cre-loxP- or CRISPR-mediated knockout of *p19*^{ARF}, *Pten*, *Prkar1a*, *Rb1*, *Cdkn1b*, and *Tsc2* , showed any cooperative effects (data not shown). However, among interrogated genes, β-catenin (using a transposon encoding *CTNNB1*^{T41A} cDNA) uniquely cooperated with *DNAJB1-PRKACA*, which we explored further. Of note, the *CTNNB1*^{T41A} is the same allele that occurred in a primary FL-HCC and its corresponding brain metastasis (**Fig. 5B, Fig. S6B)**. Both pairs of tandem guide CRISPRs, as well as transposon delivery of fusion cDNA, synergized with transposon delivery of stabilized β-catenin, increasing penetrance and reducing latency of the model (**Fig. 5C,D**). In all cases, the histology of the resulting tumors matched the single hit models, though some features (e.g. cell size) were exaggerated (**Fig. 5E**). The acceleration of the model by Wnt signaling was further validated by the combination of *DNAJB1-PRKACA* cDNA and disruption of *Apc* using CRISPR, which yielded tumors with a similar phenotype (**Fig. S7**). While expression of the *DNAJB1-PRKACA* fusion alone led to increased membranous β-catenin, and phosphorylation of β-catenin at PKA phosphorylation site S675, expression of the canonical Wnt target AXIN2 was observed only in samples with genetic manipulation of the Wnt pathway (**Fig. S7**). To further demonstrate the oncogenecity of the model, we recovered tumor tissue from a CRISPR.1 and CTNNB1 expressing tumor Addition of β-catenin did not instigate chromosomal instability, as had previously been observed in other cancer types (36, 37) (**Fig. S4**). Hence, genetic lesions that deregulate Wnt signaling can occur in the human disease and provide a unique second hit pathway that cooperates with DNAJB1-PRKACA to accelerate FL-HCC.

Inflammatory and fibrotic agent DDC enhances FL-HCC tumorigenesis

In contrast to adult HCC, FL-HCC occurs in young patients without chronic liver disease (8). Nevertheless, given that the *DNAJB1-PRKACA* fusion was insufficient to generate the eponymous fibrosis associated with the human disease, we wondered whether experimental strategies to induce fibrosis might facilitate the optimal growth of murine FL-HCC. The administration of the hepatotoxin 3,5-diethoxycarbonyl-1,4-dihydrocollidine (DDC) causes oxidative liver damage, cell death in periportal hepatocytes, atypical ductal expansion of progenitor cells, and ultimately, fibrosis (38), and can accelerate HCC tumorigenesis by specific oncogenic events (39, 40). Consistent with published results, mice treated with a 0.1% DDC-containing diet develop hepatomegaly, inflammation, and fibrosis with portal bridging by 8 weeks of treatment, but DDC alone does not generate tumors (38, 41) (**Fig. 6A-C,S8**). DDC-fed mice in which the fusion or *CTNNB1* alone was expressed formed clusters of tumor cells at an accelerated rate, and the combination of DDC, *DNAJB1-PRKACA,* and *CTNNB1* together synergized to instigate faster tumor development and more aggressive disease (**Fig. 6A,B**). The histology of the tumor cells themselves remained largely unchanged by DDC treatment, but as expected, the surrounding tissue acquired DDC-associated phenotypes associated with tissue regeneration following injury (**Fig. 6C**). Surprisingly the morbidity of the combination often preceded the establishment of significant fibrosis (**Fig. 6C,S8**). Therefore, our data suggests that one or more factors in associated with the DDC-induced regenerative response can fuel murine FL-HCC. Regardless, the use of DDC enables the production of tumor-bearing mice at high penetrance and with short latency.

Tumorigenicity of DNAJB1-PRKACA is dependent on kinase domain.

To illustrate the potential of a rapid and robust model of FL-HCC, we used the above methods to address whether the kinase activity of the *DNAJB1-PRKACA* fusion is essential for its ability to drive tumorigenesis—a prerequisite for rationalizing the use of small molecule inhibitors targeting the PRKACA kinase for treatment of FL-HCC. To this end, we produced a kinase dead version of the *DNAJB1-PRKACA* fusion harboring a mutation in the PRKACA component, equivalent to the previously described K72H mutation (42, 43), and compared its oncogenic potential to the intact fusion cDNA, when combined with DDC and *CTNNB1*^{T41A}. At approximately 10 weeks post-injection, we sacrificed a cohort of animals and examined liver lesions. While clusters of neoplastic hepatocytes with classic FL-HCC morphology were observed in samples with an intact kinase domain, no such atypical hepatocytes were identified in

samples expressing the kinase dead (KD) fusion cDNA (**Fig. 7A**). Although GFP+ cells were present in KD livers, the Ki67 index of was significantly elevated in GFP+ cells expressing the kinase intact fusion with respect to the kinase dead fusion cDNA (**Fig. 7B,C**). Thus, the PRKACA kinase domain appears required for FL-HCC tumor initiation.

Discussion

Using a combination of hydrodynamic transfection, somatic genome editing, and transposon-mediated gene delivery, we demonstrate that the *DNAJB1-PRKACA* fusion is a *bona fide* oncogene that drives FL-HCC. The loss of the intervening 400kb deleted region, encompassing 7 additional genes, is dispensable for tumorigenesis, based on tumor formation driven by ectopic expression of the fusion cDNA. The gene fusion appears to be functionally distinct from the mere overexpression of wild type *PRKACA*, which is insufficient for oncogenesis when overexpressed in adult hepatocytes. On the other hand, the kinase domain of PRKACA is required for the FL-HCC phenotype. Importantly, this indicates the potentially druggable enzymatic activity of the chimera is important for tumorigenesis.

Numerous features of these FL-HCC models mimic the human disease. Histologically, our methods generate tumors whose morphology is strikingly reminiscent of human FL-HCC. Dramatic accumulation of mitochondria appears to be a consistent consequence of DNAJB1-PRKACA activity, further linking our model to the human disease. Globally, we observe an expression signature significantly enriched for the genes differentially expressed in human FL-HCC.

In addition to the DNABJ1-PRKACA fusion, we note that some FL-HCC tumors have secondary mutations in components of the Wnt signaling pathway and that genetic alteration of this pathway– but not several other oncogenes or tumor suppressors —synergizes with DNAJB1-PRKACA-driven tumorigenesis. The mechanism for this interaction is unclear, but several possibilities exist. First, β-catenin may be one downstream output of DNAJB1-PRKACA, and stabilization of β-catenin may amplify its functional consequences. PKA has been described to regulate β-catenin through a variety of mechanisms, including direct stabilization via C-terminal phosphorylation (44-46). Accordingly, the levels of phospho-β-catenin at Y654 were highly elevated in human FL-HCC samples with respect to other HCC samples, which is likely related to PKA (47, 48). Alternatively, β-catenin may protect cells from oxidative stress imposed by DNAJB1-PRKACA (49), or β-catenin may be enforcing a progenitor-like state associated with more efficient transformation by *DNAJB1-PRKACA*.

The ability of DDC to accelerate DNAJB1-PRKACA driven tumorigenesis was unexpected but had dramatic effects on the latency of the model. By causing oxidative stress-induced cell death in a subset of pericentral hepatocytes, DDC sets in motion a liver regenerative response that is associated with compensatory expansion of liver progenitor cells, activation of myofibroblasts, and massive immune cell infiltration (41) in a process supported by hepatocyte expression of β-catenin (49). Any or all of the activated and recruited cell types could contribute paracrine signals that protect and stimulate growth in the spatially separated (largely pericentral) population of hepatocytes that are transfected by hydrodynamic injection (31). While chronic liver damage is not considered to be necessary for human FL-HCC, our data raise the possibility that some environmental factor, perhaps in a susceptible population, may be relevant in the etiology of the disease. Alternatively, as our study used adult mice, it could be that β-catenin and/or DDC facilitated a change in hepatocyte cell state that supports or expands a progenitor cell population more prevalent in adolescents and prone to *DNAJB1-PRKACA*-induced oncogenesis.

Animal models set a gold standard for assessing the oncogenic potential of aberrations observed in human cancer. They also provide an opportunity to delve into mechanisms of pathogenesis, search for biological processes that support tumor progression or candidate drug targets, and characterize tumor-host interactions (14). Somatic genome editing of autochthonous mouse models has the potential to open up the opportunity to study a wider array of genetic events than ever before possible (50). The methods described here do not require viral delivery of Cas9, generating new strains of mice, or transplantation of cells modified *in vitro*. Our approaches deliver only plasmid DNA to hepatocytes and drive transformation *in situ*. A patient-derived xenograft (PDX) of FL-HCC has been described (51), and the opportunity to study human tumor tissue *in vivo* is valuable, our models introduce the ability to examine the entire process of tumor initiation in immune competent organisms. Our model is easily implemented, reproducible, and genetically defined. As it is based on commercially available wild type mice, it does not

require expensive and time-consuming breeding schemes. This approach allows for the synchronous generation of large cohorts of mice for survival and intervention studies. We anticipate that the systems described here will provide powerful platforms to further understand the biology of FL-HCC and empower drug discovery for a disease with severely limited treatment options that disproportionately affects young patients.

Materials and Methods

Vectors and cloning

One sgRNA was cloned into the px330 vector, which was a gift from Feng Zhang (Addgene plasmid # 42230) (52), and a second U6-sgRNA cassette was inserted in the XbaI site with XbaI-NheI overhangs. As indicated, for other experiments (**Fig. S1**), the lenti-CRISPR vector was a gift from David Sabatini (Addgene plasmid # 70662) (53). The pT3 transposon and SBase vectors were a kind gift of Dr. Xin Chen, University of California at San Francisco. Sequences for sgRNAs, cDNAs and primers are listed in **Supplementary Table 4**.

Animals and Treatments

Female, 8- to 10-week-old C57BL6/N mice were purchased from Envigo (East Millstone, NJ). All animal experiments were approved by the MSKCC Institutional Animal Care and Use Committee (protocol 11-06-011). For hydrodynamic tail-vein injection, a sterile 0.9% NaCl solution was prepared containing plasmid DNA of either 40µg CRISPR vector or 20µg transposon vector together with CMV-SB13 Transposase (1:5 molar ratio). Mice were injected into the lateral tail vein with a total volume corresponding to 10% of body weight (typically 2 ml for a 20g mouse) in 5–7 seconds (15, 54). DDC treatment was accomplished by feeding mice a diet containing 0.1% DDC (Sigma-Aldrich, St. Louis, Missouri; Envigo, Madison, WI) until sacrifice (40).

Electron Microscopy

Tissue was fixed in 4% glutaraldehyde and transferred to cold PBS until further processed. The tissues were post fixed in 1% osmium tetroxide in PBS. After washing in water, the tissue was stained with 2% aqueous uranyl acetate for ~2 h at 4°. Tissues were dehydrated through a series of acetones and propylene oxide and embedded in Epon. Ultrathin sections were deposited on grids and stained with uranyl acetate for 15 minutes and lead citrate for 5 minutes.

Immunohistochemistry and Immunofluorescence

Tissue was prepared for histology by fixing in 10% buffered formalin overnight then transferred to 70% ethanol until paraffin embedding and sectioning (IDEXX RADIL, Columbia, MO). Antigen retrieval was performed in a pressure cooker with Sodium Citrate buffer. Primary antibodies were incubated at 4°C overnight in blocking buffer. Sections were incubated with anti-rabbit ImmPRESS HRP-conjugated secondary antibodies (Vector Laboratories, #MP7401) and chromagen development performed using ImmPact DAB (Vector Laboratories, #SK4105). Stained slides were counterstained with Harris' hematoxylin. Images of stained sections were acquired on a Zeiss Axioscope Imager Z.1 and an ORCA/ER CCD camera (Hamamatsu Photonics, Hamamatsu, Japan). Raw .tif files were processed using Photoshop CS5 software (Adobe Systems Inc., San Jose, CA) to adjust white balance.

RNAseq

Total RNA was isolated from frozen tissue using the RNeasy Mini Kit (Qiagen), quality control was performed on an Agilent BioAnalyzer, 500 ng of total RNA (RNA integrity number>8) underwent polyA selection and Truseq library preparation according to instructions provided by Illumina (TruSeq RNA Sample Prep Kit v.2) with 6 cycles of PCR. Single-end, 75-bp sequencing was performed at the CSHL core facility. Approximately 8 million reads were acquired per sample. Resulting RNA-Seq data was analyzed as described previously (23). Adaptor sequences were removed using Trimmomatic. RNA-seq reads were then aligned to the mouse genome (mm10) using STAR (55) with default parameters and

genome-wide transcript counting was performed using subread to generate a count matrix (56, 57). Differential expression analysis was performed by DESeq2 (58). Genes were considered to be significantly differentially expressed if tumor/normal comparison was greater than 2-fold and FDR-adjusted p value was less than 0.05.

Human-Murine mapping of orthologs was performed based on the Ensembl database accessed through the Biomart R/Bioconductor package (59). Human fibrolamellar HCC signatures were set as genes with at least 2-fold and significant expression changes in fibrolamellar tumors with respect to normal. Human transcriptional profiling data was obtained from published studies (7, 29), and the TCGA/Broad GDAC firehose using annotation from Dinh et al (10). For comparison to human datasets and for gene set enrichment analysis, the ssGSEA method was implemented using the GSVA package within R (28). The GSVA outputs were subsequently compared across groups using the limma package (60). The C2, C3, C5, and Hallmark collections of gene sets from MSigDBv6.0 were queried (61).

Copy Number Profiling

Low-pass whole genome sequencing was used to determine tumor copy number profiles as described previously (23). One microgram of DNA per sample was sonicated (17 W, 75 s) on an E220 sonicator (Covaris), prepared using standard Illumina library preparation, purified using AMPure XP magnetic beads (Beckman Coulter), PCR enriched, and sequenced on an Illumina HiSeq instrument in a multiplexed format. Sequencing reads per sample were mapped using Bowtie with PCR duplicates removed. Approximately 2.5 million uniquely mappable reads were further processed for copy number determination using the 'varbin' algorithm with 5,000 bins, allowing for a median resolution of approximately 600 kb after GC content normalization, segmentation and copy number estimation (62).

Human Tumor Sequencing Data

The MSK-IMPACT sequencing data (35) were obtained from the MSKCC cBioPortal (63) (http://www.cbioportal.org). Of the 18 *DNAJB1-PRKACA* fusion cases, 14 were annotated as fibrolamellar HCC and 4 were annotated as HCC. We considered all *DNAJB1-PRKACA* positive liver cancers as FL-HCC, given the common of misdiagnosis of this rare cancer type (10), for which the presence of the *DNAJB1-PRKACA* should be considered diagnostic (2).

Figure Legends

Fig. 1. CRISPR-mediated deletion results in fusion oncogene and drives tumorigenesis in vivo. (**A**) Configuration of human chromosome 19, including *DNAJB1* and *PRKACA*, configuration of mouse chromosome 8, including *Dnajb1* and *Prkaca*, and schematic of endogenous 400kb deletion targeted by hydrodynamic injection of vector containing tandem guide sgRNAs to introns of *Dnajb1* and *Prkaca* and Cas9. (**B**) Overall survival of mice injected with indicated tandem guide CRISPRs. (**C**) Macroscopic view of a tumor-bearing liver (**D**) Fraction of mice harvested with no detectable tumor, asymptomatic mice with histologically detectable disease (asymptomatic), or moribund mice with tumors (moribund) for each indicated genotype. (**E**) Sanger sequencing of chimeric transcript amplified tumor generated CRISPR.1 (top) and CRISPR.2 (bottom). (**F**) H&E staining of tumor generated by CRISPR.1 (top) and CRISPR.2 (bottom). (**G**) Human case of FL-HCC (T, tumor; F, fibrosis). (**H**) Normal mouse liver (CV, central vein; PV, portal vein) with intact sinusoids (white line, s). All scale bars are 50 µm.

Fig. 2. DNAJB1-PRKACA fusion protein drives liver tumorigenesis. (**A**) Schematic of Sleeping Beauty transposon strategy to deliver *DNAJB1-PRKACA* fusion cDNA to young adult livers. (**B**) Overall survival of mice injected with cDNA encoding fusion protein, wild-type *PRKACA*, or empty vector. (**C**) Fraction of mice harvested with no detectable tumor, asymptomatic mice with histologically detectable disease, or moribund mice with tumors expressing empty vector (EV), wild type *PRKACA*, or *DNAJB1-PRKACA* fusion. (**D**) Western blot of 293 cells transfected with indicated constructs *in vitro* (**E**) Tumor generated by pT3-DNAJB1-PRKACA (T, tumor; N, adjacent normal; scale bar=50um). (**F**) Higher magnification image highlighting: *i.* caniculus-like lumen, *ii.* multi-nucleated, *iii.* granular, eosinophilic cytoplasm, *iv.* bile accumulation, *v.* Mallory body, *vi.* aneuploid cell with coarsely clumped chromatin . Inset: *vii.* pale body. All scale bars are 50 µm.

Fig. 3. Molecular characterization of murine FL-HCC. Ultrastructural analysis of a transposon-induced tumor by electron microscopy (**A**) normal compressed hepatocytes adjacent to FL-HCC. (**B**) FL-HCC tumor cells are enlarged with abnormally abundant mitochondria (yellow arrowhead). Necrotic cells (blue) and nonfenestrated vessels (orange), and indistinct cell-cell junctions (black). (**C**) Higher magnification of adjacent normal hepatocytes (green) compressed at the tumor margin (tumor cell, black) (**D**) Perinuclear accumulation of lipofuscin (black) and heterochromatin (white). (**E**) Tumor cells with abundant mitochondria (yellow), Rough endoplasmic reticulum (RER, red) and simple cell-cell junctions. (**F**) Abnormal mitochondria (yellow) with indistinct cristae surrounded in RER (red). (**G**) E-cadherin (CDH1) staining (left column) of CRISPR-induced tumor (top), or transposon-induced tumor (bottom). Periodic Acid Schiff (PAS) staining (middle column). Note adjacent normal hepatocytes positive with asymmetrical subcellular distribution (black arrow) compared to tumor with negative or weak and distributed staining. (T, tumor; N, normal). β-catenin (CTNNB1) staining (right column). Scale bars for **G** are 50 µm.
Fig. 4. Murine FL-HCC exhibits a physiologically relevant transcriptomal signature. (**A**) Principal component analysis of young control livers (dark blue), aged control livers (light blue), and tumors derived from CRISPR.1 (red). (**B**) Z scored single sample gene set enrichment analysis (ssGSEA) for normal (black) and tumor (red) samples. **P<0.01 ***P<0.001. (**C**) Volcano plot depicting differentially expressed genes. (**D**) ssGSEA analysis for select functionally annotated gene sets.
Fig. 5. WNT pathway cooperates with fusion to accelerate FL-HCC tumorigenesis.
(A) Frequency of top 10 most commonly mutated genes in hepatocellular carcinoma (HCC, n=142), intrahepatic cholangiocarcinoma (ICC, n=175), and fibrolamellar carcinoma (FLHCC, n=18) from MSKCC IMPACT sequencing. (**B**) Domain schematic of loci of Wnt pathway mutations in FL-HCC.
(**C**) Overall survival of mice of indicated genotypes with or without pT3-CTNNB1. CRISPR.1, CRISPR.2, and DNAJB1-PRKACA are repeated from (**Figs. 1-2**) (**D**) Fraction of mice harvested with no detectable tumor, asymptomatic mice with histologically detectable disease (asymptomatic), or moribund mice with tumors (moribund) for each indicated genotype. (**E**) H & E images depicting histology of mice injected with pT3-CTNNB1 in combination with CRISPR.1, CRISPR.2, or pT3-chimera

Fig. 6. Inflammatory and fibrotic agent DDC supports FL-HCC tumorigenesis.
(**A**) Overall survival of mice injected with indicated genotypes and/or fed DDC diet. Survival data of mice without DDC treatment repeated from (**Figs. 1,2,5**) (**B**) Fraction of mice harvested with no detectable tumor, asymptomatic mice with histologically detectable disease (asymptomatic), or moribund mice with tumors (moribund) for each indicated genotype with or without DDC diet. (**c**) H & E images depicting histology of mice of the indicated genotypes and fed DDC diet.

Supplementary Figure Legends
Fig. S1. Validation of CRISPR-mediated deletion. (A) Schematic of sgRNAs and primers. **(B)** Detection of genomic deletion in NIH-3T3 cells infected with tandem guide lentiCRISPR construct. (**C**) Detection of deletion in genomic DNA extracts from whole livers 4 days following hydrodynamic tail vein injection of the same construct. (**D**) Overall survival of mice following hydrodynamic tail vein injection of the lentiCRISPR plasmid DNA.
Fig. S2. Additional ultrastructural analysis of murine FL-HCC. (A) lower magnification image of Fig. 3b, showing side-by-side tumor cells (black arrows) of varying larger size than compressed adjacent hepatocytes at tumor margin (green arrows). **(B)** Simple, non-distinct cell-cell junctions (black arrows) **(C)** rare desmosome “d” with nearby sinusoid “s” **(D)** tumor-associated vasculature (black arrow) **(E-H)** Abundant mitochondria (yellow arrows) surrounded by rough endoplasmic reticulum (red arrows) with scant smooth endoplasmic reticulum **(I)** Lipofuscin “Lf” **(J,K)** Tumor nuclei are large and round to indented with prominent nucleoli (white arrows) **(L)** Bile canniculi are sometimes widened (black arrows).
Fig. S3. Additional molecular characterization of murine FL-HCC. Indicated genotypes stained for hepatocyte markers (**A**) HNF1A and (**B**) HNF4A, cholangiocyte markers (**C**) CK7 and (**D**) CK19, (**E**) CD68 indicating positive infiltrating macrophages and negative tumor cells and (**F**) IBA1 confirming **E**. Black arrows indicate bile ducts. All scale bars are 50 µm.
Fig. S4. Copy number profiling of murine FL-HCC.

Low-pass whole genome sequencing was performed and data was binned into 5000 segments for (**A**) a tumor generated by a transposon expressing DNAJB1-PRKACA and (**B**) a tumor generated by the combination of transposons expressing DNAJB1-PRKACA and CTNNB1.

Fig. S5. Gene expression of FL-HCC-associated gene sets of interest. (A) ssGSEA enrichment scores from mouse tumor differential expression (homologs converted to human genes) for gene sets significantly enriched in either upregulated or downregulated human gene expression data (29) (p=4.22-17). **(B)** Gene expression for genes encoded by mitochondrial DNA. Gene expression of corresponding mouse and human (29) genes in the specified gene sets: **(C)** CREB targets **(D)** Wnt signaling pathway **(E)** GRB2 events in ERBB2 signaling **(F)** genes upregulated by ROS **(G)** Lineage specific genes including neuroendocrine markers (29) and (**H**) liver zone-specific genes (30).

Fig. S6. Wnt pathway alteration in human FL-HCC. (**A**) Age distribution of patients with the indicated types of liver tumors (HCC n=129, ICC n=165, FLHCC n=16). (**B**) Clinical and genomic characteristics of 3 cases of FL-HCC with Wnt pathway mutation.

Fig. S7. Wnt pathway in murine FL-HCC.

Staining of livers injected with pT3-DNAJB1-PRKACA, pT3-CTNNB1, the combination of pT3-DNAJB1-PRKACA and pT3-CTNNB1, or the combination of CRISPR.1 and pT3-CTNNB1 with (**A**) H&E or immunohistochemistry with antibodies against (**B**) Ctnnb1, (**C**) p-Ctnnb1 S675 (PKA target site), and (**D**) Axin2 (Wnt target gene). CV=Central vein (AXIN2 internal positive control). All scale bars are 50 µm.

Fig. S8. Fibrosis following DDC. Trichrome staining indicating mild fibrosis in livers from mice following DDC treatment and injection with the indicated constructs.

Author contributions

E.R.K. performed experiments, analyzed results, performed data analysis and wrote the paper. G.L. and T.B. coordinated experiments and analyzed results. D.F.T., S.L.H., and B.B. provided critical reagents, technical advice and planned experiments. S.T. performed experiments. T.B. performed experiments and performed data analysis of copy number profiling data. C.C. and D.R.E. performed data analysis. J.E.W. performed electron microscopy and provided pathology expertise. S.M.S. conceived the project, supervised experiments, analyzed results, and wrote the paper. S.W.L. conceived the project, supervised experiments, analyzed results, and wrote the paper.

Acknowledgements

We would like to thank Francisco Sanchez-Rivera (MSKCC), Yadira Soto-Feliciano (Rockefeller University), and John P. Morris IV (MSKCC) for critical reading of the manuscript, and all members of the Lowe laboratory for advice and discussions. We thank Wei Luan and Leah Zamachek for technical assistance and Joana DeCampos Vidigal and Andrea Ventura for critical insights. This work was supported primarily by a project grant from the Starr Cancer Consortium (I10-0098) to S.W.L. and S.M.S. This study was also supported in part by NIH National Cancer Institute (NCI) grant P30 CA008748 (Cancer Center Support Grant). E.R.K. is supported by an F31 NRSA predoctoral fellowship from the NCI/National Institutes of Health under award number F31CA192835. G.L., D.R.A. and S.M.S. were supported by a grant from the NIH 1R56CA207929. S.W.L. is an investigator of the Howard Hughes Medical Institute and the Geoffrey Beene Chair for Cancer Biology.

References

1. Honeyman JN*, et al.* (2014) Detection of a recurrent DNAJB1-PRKACA chimeric transcript in fibrolamellar hepatocellular carcinoma. *Science* 343(6174):1010-1014.
2. Graham RP*, et al.* (2015) DNAJB1-PRKACA is specific for fibrolamellar carcinoma. *Mod Pathol* 28(6):822-829.
3. Priya S, Sharma SK, & Goloubinoff P (2013) Molecular chaperones as enzymes that catalytically unfold misfolded polypeptides. *FEBS Lett* 587(13):1981-1987.

4. Turnham RE & Scott JD (2016) Protein kinase A catalytic subunit isoform PRKACA; History, function and physiology. *Gene* 577(2):101-108.
5. Cheung J*, et al.* (2015) Structural insights into mis-regulation of protein kinase A in human tumors. *Proceedings of the National Academy of Sciences of the United States of America* 112(5):1374-1379.
6. Darcy DG*, et al.* (2015) The genomic landscape of fibrolamellar hepatocellular carcinoma: whole genome sequencing of ten patients. *Oncotarget* 6(2):755-770.
7. Cornella H*, et al.* (2015) Unique genomic profile of fibrolamellar hepatocellular carcinoma. *Gastroenterology* 148(4):806-818 e810.
8. Torbenson M (2012) Fibrolamellar carcinoma: 2012 update. *Scientifica (Cairo)* 2012:743790.
9. Graham RP*, et al.* (2017) Environmental exposures as a risk factor for fibrolamellar carcinoma. *Mod Pathol* 30(6):892-896.
10. Dinh TA*, et al.* (2017) Comprehensive analysis of The Cancer Genome Atlas reveals a unique gene and non-coding RNA signature of fibrolamellar carcinoma. *Sci Rep* 7:44653.
11. Kaseb AO*, et al.* (2013) Prognostic indicators and treatment outcome in 94 cases of fibrolamellar hepatocellular carcinoma. *Oncology* 85(4):197-203.
12. Eggert T*, et al.* (2013) Fibrolamellar hepatocellular carcinoma in the USA, 2000-2010: A detailed report on frequency, treatment and outcome based on the Surveillance, Epidemiology, and End Results database. *United European Gastroenterol J* 1(5):351-357.
13. Riggle KM, Turnham R, Scott JD, Yeung RS, & Riehle KJ (2016) Fibrolamellar Hepatocellular Carcinoma: Mechanistic Distinction From Adult Hepatocellular Carcinoma. *Pediatr Blood Cancer* 63(7):1163-1167.
14. Kersten K, de Visser KE, van Miltenburg MH, & Jonkers J (2017) Genetically engineered mouse models in oncology research and cancer medicine. *EMBO Mol Med* 9(2):137-153.
15. Tschaharganeh DF*, et al.* (2014) p53-dependent Nestin regulation links tumor suppression to cellular plasticity in liver cancer. *Cell* 158(3):579-592.
16. Kawakami K, Largaespada DA, & Ivics Z (2017) Transposons As Tools for Functional Genomics in Vertebrate Models. *Trends Genet*.
17. Maddalo D*, et al.* (2014) In vivo engineering of oncogenic chromosomal rearrangements with the CRISPR/Cas9 system. *Nature* 516(7531):423-427.
18. Cook PJ*, et al.* (2017) Somatic chromosomal engineering identifies BCAN-NTRK1 as a potent glioma driver and therapeutic target. *Nat Commun* 8:15987.
19. Han T*, et al.* (2017) R-Spondin chromosome rearrangements drive Wnt-dependent tumour initiation and maintenance in the intestine. *Nat Commun* 8:15945.
20. Choi PS & Meyerson M (2014) Targeted genomic rearrangements using CRISPR/Cas technology. *Nat Commun* 5:3728.
21. Blasco RB*, et al.* (2014) Simple and rapid in vivo generation of chromosomal rearrangements using CRISPR/Cas9 technology. *Cell Rep* 9(4):1219-1227.
22. Engelholm LH*, et al.* (2017) CRISPR/Cas9 Engineering of Adult Mouse Liver Demonstrates That the Dnajb1-Prkaca Gene Fusion is Sufficient to Induce Tumors Resembling Fibrolamellar Hepatocellular Carcinoma. *Gastroenterology*.
23. Liu Y*, et al.* (2016) Deletions linked to TP53 loss drive cancer through p53-independent mechanisms. *Nature* 531(7595):471-475.
24. Payne CM, Nagle RB, Paplanus SH, & Graham AR (1986) Fibrolamellar carcinoma of liver: a primary malignant oncocytic carcinoid? *Ultrastruct Pathol* 10(6):539-552.
25. Ward SC*, et al.* (2010) Fibrolamellar carcinoma of the liver exhibits immunohistochemical evidence of both hepatocyte and bile duct differentiation. *Mod Pathol* 23(9):1180-1190.
26. Ross HM*, et al.* (2011) Fibrolamellar carcinomas are positive for CD68. *Mod Pathol* 24(3):390-395.
27. Zhang M*, et al.* (2014) Protein kinase A activation enhances beta-catenin transcriptional activity through nuclear localization to PML bodies. *PLoS One* 9(10):e109523.
28. Hanzelmann S, Castelo R, & Guinney J (2013) GSVA: gene set variation analysis for microarray and RNA-seq data. *BMC Bioinformatics* 14:7.

29. Simon EP*, et al.* (2015) Transcriptomic characterization of fibrolamellar hepatocellular carcinoma. *Proceedings of the National Academy of Sciences of the United States of America* 112(44):E5916-5925.
30. Halpern KB*, et al.* (2017) Single-cell spatial reconstruction reveals global division of labour in the mammalian liver. *Nature* 542(7641):352-356.
31. Chen X & Calvisi DF (2014) Hydrodynamic transfection for generation of novel mouse models for liver cancer research. *Am J Pathol* 184(4):912-923.
32. Luo C*, et al.* (2013) Mitochondrial accumulation under oxidative stress is due to defects in autophagy. *J Cell Biochem* 114(1):212-219.
33. Sohal RS & Brunk UT (1989) Lipofuscin as an indicator of oxidative stress and aging. *Adv Exp Med Biol* 266:17-26; discussion 27-19.
34. Hohn A, Sittig A, Jung T, Grimm S, & Grune T (2012) Lipofuscin is formed independently of macroautophagy and lysosomal activity in stress-induced prematurely senescent human fibroblasts. *Free Radic Biol Med* 53(9):1760-1769.
35. Zehir A*, et al.* (2017) Mutational landscape of metastatic cancer revealed from prospective clinical sequencing of 10,000 patients. *Nat Med* 23(6):703-713.
36. Hadjihannas MV*, et al.* (2006) Aberrant Wnt/beta-catenin signaling can induce chromosomal instability in colon cancer. *Proceedings of the National Academy of Sciences of the United States of America* 103(28):10747-10752.
37. Aoki K*, et al.* (2007) Chromosomal instability by beta-catenin/TCF transcription in APC or beta-catenin mutant cells. *Oncogene* 26(24):3511-3520.
38. Preisegger KH*, et al.* (1999) Atypical ductular proliferation and its inhibition by transforming growth factor beta1 in the 3,5-diethoxycarbonyl-1,4-dihydrocollidine mouse model for chronic alcoholic liver disease. *Lab Invest* 79(2):103-109.
39. Matter MS*, et al.* (2016) Oncogenic driver genes and the inflammatory microenvironment dictate liver tumor phenotype. *Hepatology* 63(6):1888-1899.
40. Beer S*, et al.* (2008) Hepatotoxin-induced changes in the adult murine liver promote MYC-induced tumorigenesis. *PLoS One* 3(6):e2493.
41. Fickert P*, et al.* (2007) A new xenobiotic-induced mouse model of sclerosing cholangitis and biliary fibrosis. *Am J Pathol* 171(2):525-536.
42. Iyer GH, Moore MJ, & Taylor SS (2005) Consequences of lysine 72 mutation on the phosphorylation and activation state of cAMP-dependent kinase. *J Biol Chem* 280(10):8800-8807.
43. Moody SE*, et al.* (2015) PRKACA mediates resistance to HER2-targeted therapy in breast cancer cells and restores anti-apoptotic signaling. *Oncogene* 34(16):2061-2071.
44. Kang DE*, et al.* (2002) Presenilin couples the paired phosphorylation of beta-catenin independent of axin: implications for beta-catenin activation in tumorigenesis. *Cell* 110(6):751-762.
45. Hino S, Tanji C, Nakayama KI, & Kikuchi A (2005) Phosphorylation of beta-catenin by cyclic AMP-dependent protein kinase stabilizes beta-catenin through inhibition of its ubiquitination. *Mol Cell Biol* 25(20):9063-9072.
46. Fang X*, et al.* (2000) Phosphorylation and inactivation of glycogen synthase kinase 3 by protein kinase A. *Proceedings of the National Academy of Sciences of the United States of America* 97(22):11960-11965.
47. Cieply B, Zeng G, Proverbs-Singh T, Geller DA, & Monga SP (2009) Unique phenotype of hepatocellular cancers with exon-3 mutations in beta-catenin gene. *Hepatology* 49(3):821-831.
48. van Veelen W*, et al.* (2011) beta-catenin tyrosine 654 phosphorylation increases Wnt signalling and intestinal tumorigenesis. *Gut* 60(9):1204-1212.
49. Tao GZ*, et al.* (2013) Wnt/beta-catenin signaling protects mouse liver against oxidative stress-induced apoptosis through the inhibition of forkhead transcription factor FoxO3. *J Biol Chem* 288(24):17214-17224.
50. Sanchez-Rivera FJ*, et al.* (2014) Rapid modelling of cooperating genetic events in cancer through somatic genome editing. *Nature* 516(7531):428-431.

51. Oikawa T*, et al.* (2015) Model of fibrolamellar hepatocellular carcinomas reveals striking enrichment in cancer stem cells. *Nat Commun* 6:8070.
52. Cong L*, et al.* (2013) Multiplex genome engineering using CRISPR/Cas systems. *Science* 339(6121):819-823.
53. Wang T*, et al.* (2015) Identification and characterization of essential genes in the human genome. *Science* 350(6264):1096-1101.
54. Bell JB*, et al.* (2007) Preferential delivery of the Sleeping Beauty transposon system to livers of mice by hydrodynamic injection. *Nat Protoc* 2(12):3153-3165.
55. Dobin A*, et al.* (2013) STAR: ultrafast universal RNA-seq aligner. *Bioinformatics* 29(1):15-21.
56. Liao Y, Smyth GK, & Shi W (2013) The Subread aligner: fast, accurate and scalable read mapping by seed-and-vote. *Nucleic Acids Res* 41(10):e108.
57. Liao Y, Smyth GK, & Shi W (2014) featureCounts: an efficient general purpose program for assigning sequence reads to genomic features. *Bioinformatics* 30(7):923-930.
58. Love MI, Huber W, & Anders S (2014) Moderated estimation of fold change and dispersion for RNA-seq data with DESeq2. *Genome Biol* 15(12):550.
59. Durinck S, Spellman PT, Birney E, & Huber W (2009) Mapping identifiers for the integration of genomic datasets with the R/Bioconductor package biomaRt. *Nat Protoc* 4(8):1184-1191.
60. Ritchie ME*, et al.* (2015) limma powers differential expression analyses for RNA-sequencing and microarray studies. *Nucleic Acids Res* 43(7):e47.
61. Liberzon A*, et al.* (2015) The Molecular Signatures Database (MSigDB) hallmark gene set collection. *Cell Syst* 1(6):417-425.
62. Baslan T*, et al.* (2012) Genome-wide copy number analysis of single cells. *Nat Protoc* 7(6):1024-1041.
63. Cerami E*, et al.* (2012) The cBio cancer genomics portal: an open platform for exploring multidimensional cancer genomics data. *Cancer Discov* 2(5):401-404.

Figure 1. CRISPR-mediated deletion results in fusion oncogene and tumorigenesis *in vivo*.

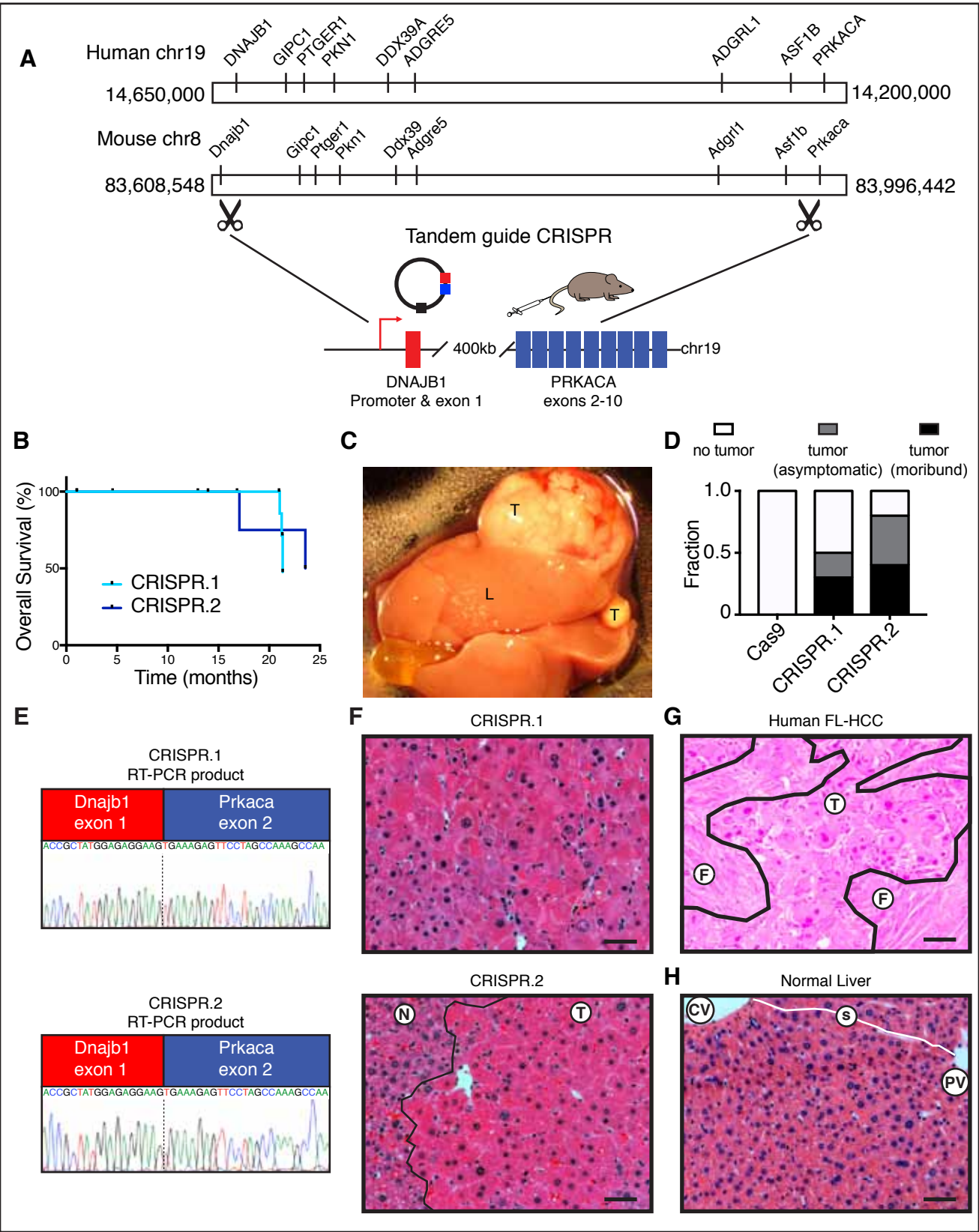

Figure 2. DNAJB1-PRKACA fusion protein drives liver tumorigenesis.

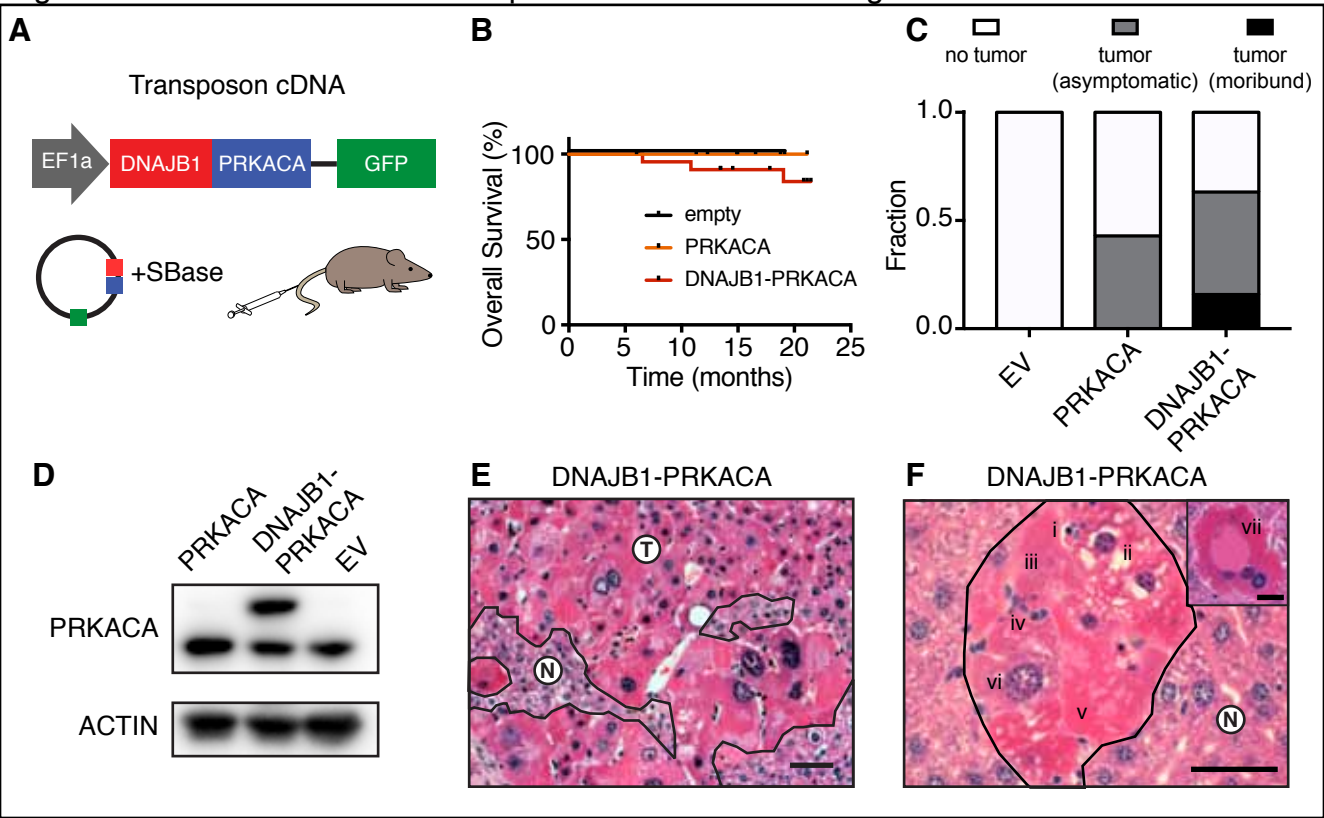

Figure 3. Molecular characterization of murine FL-HCC.

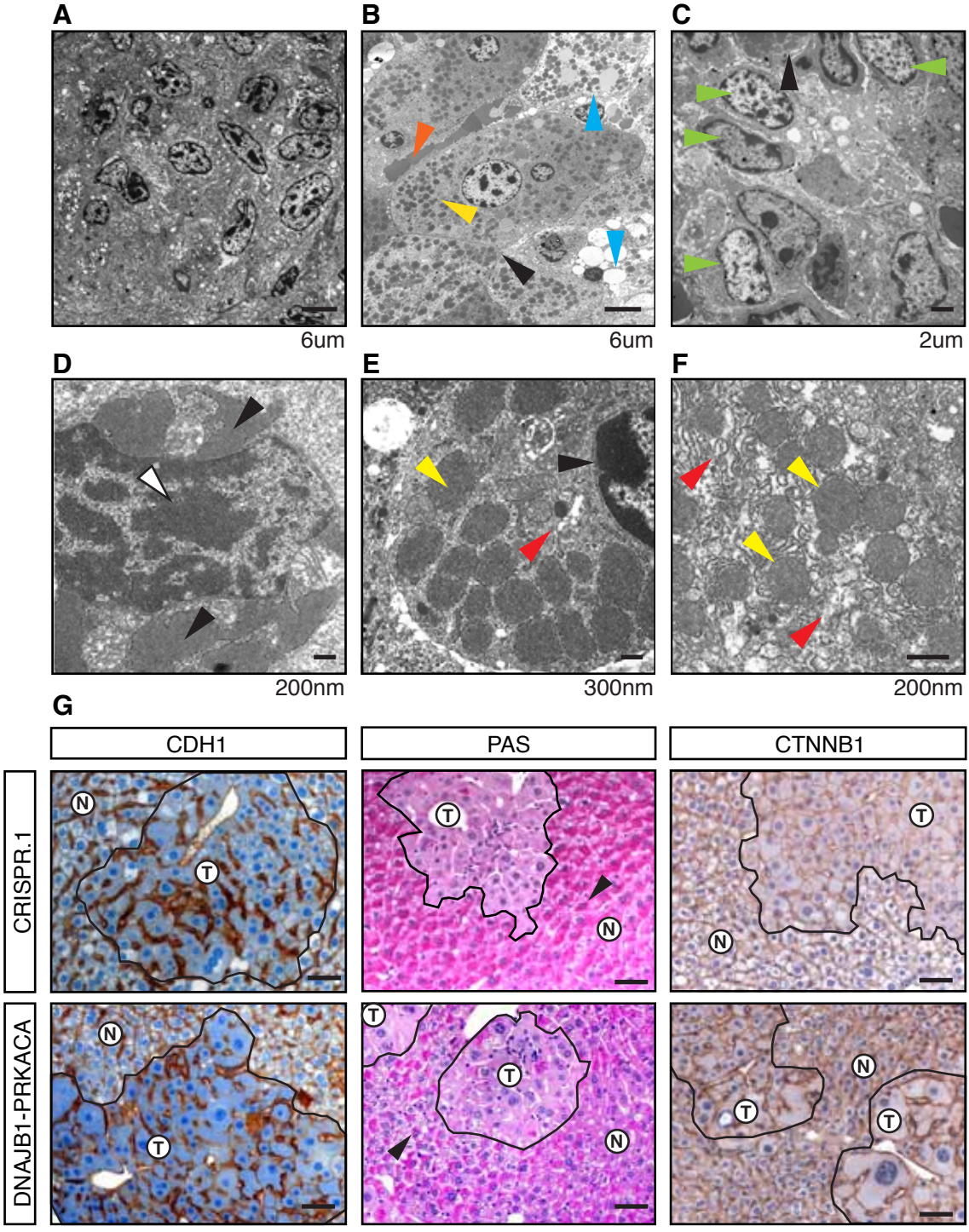

Figure 4. Murine FL-HCC exhibits a physiologically relevant transcriptomal signature.

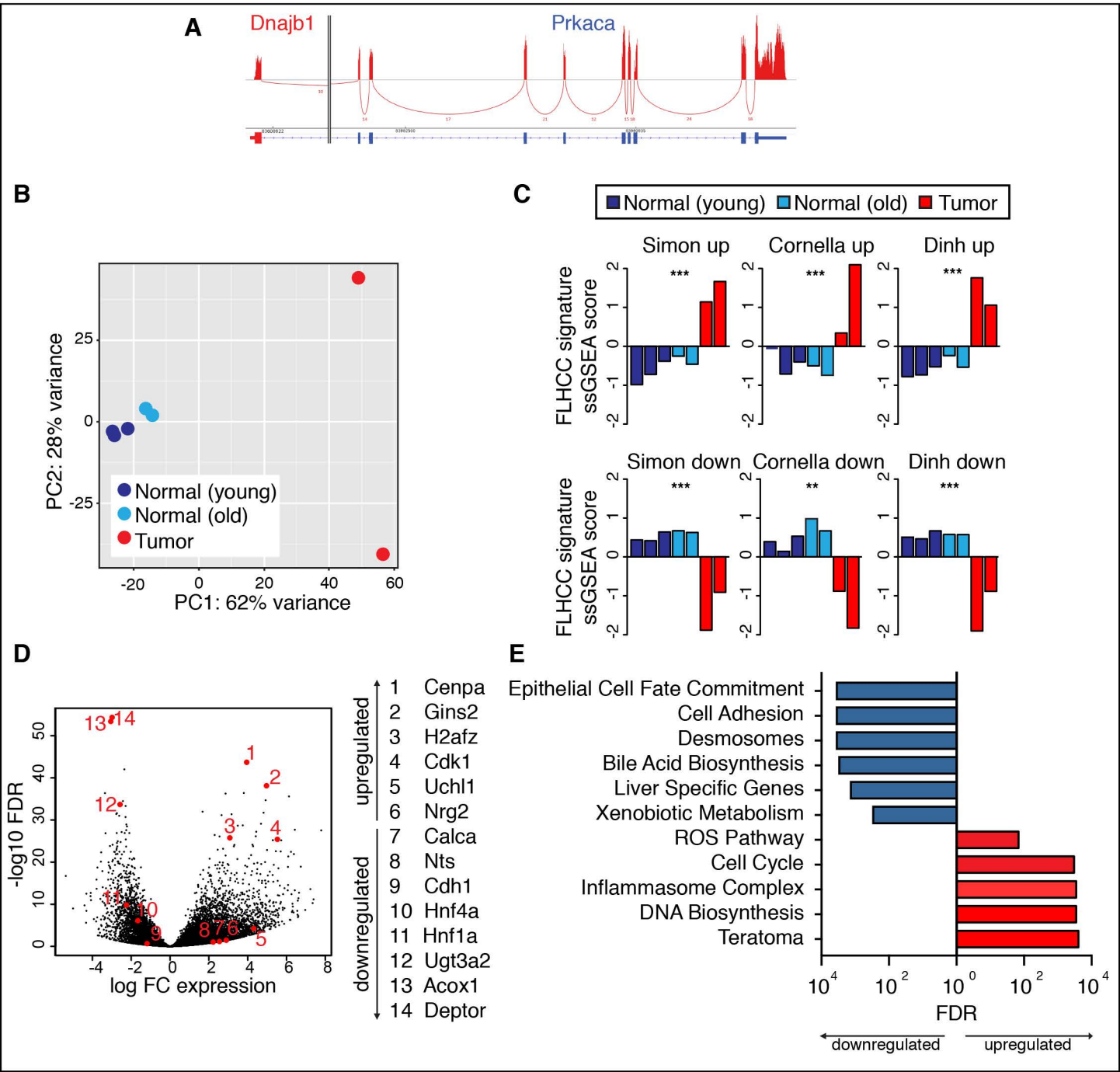

Figure 5. WNT pathway cooperates with fusion to accelerate FL-HCC tumorigenesis.

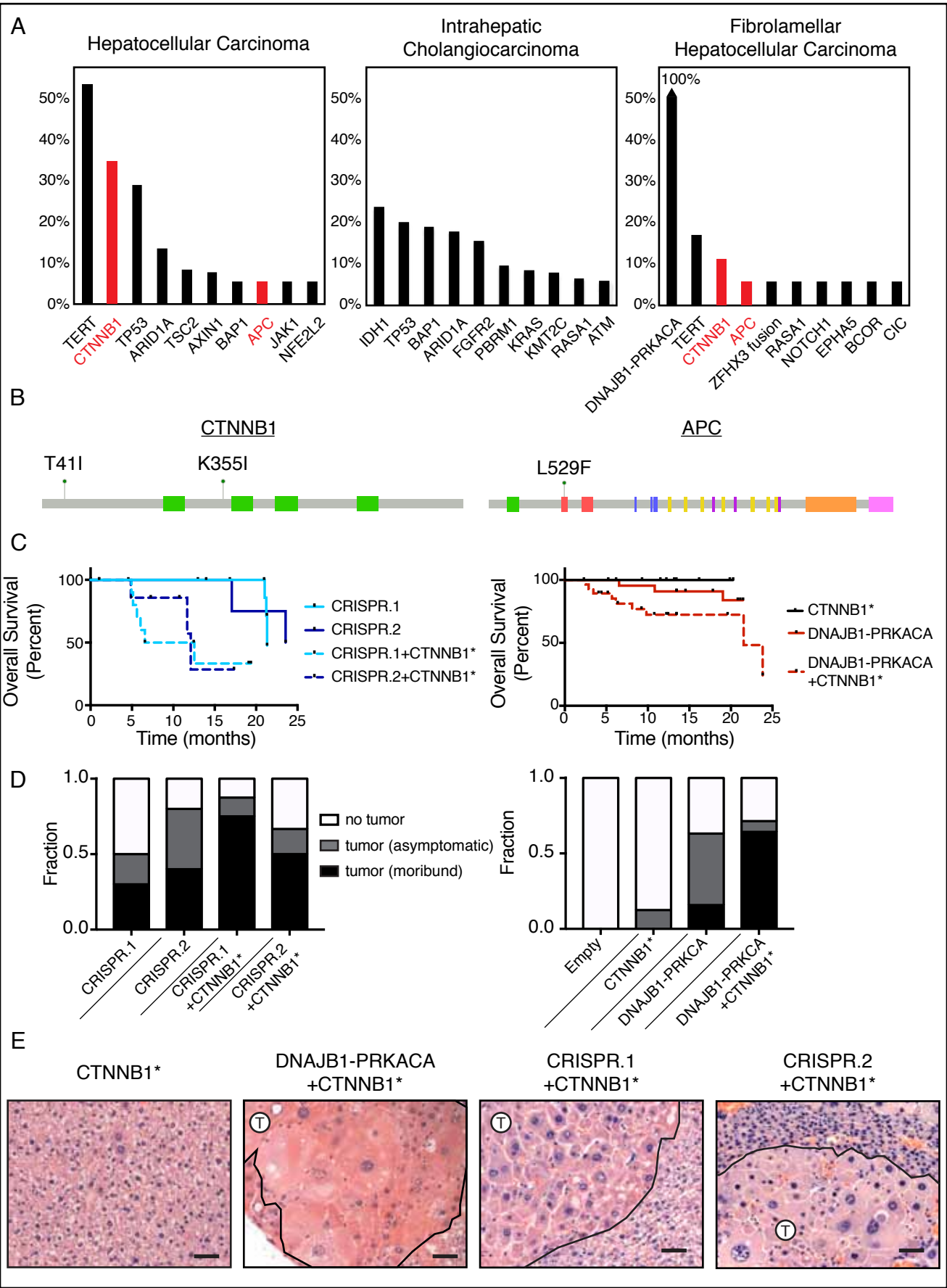

Figure 6. Inflammatory and fibrotic agent DDC supports FL-HCC tumorigenesis.

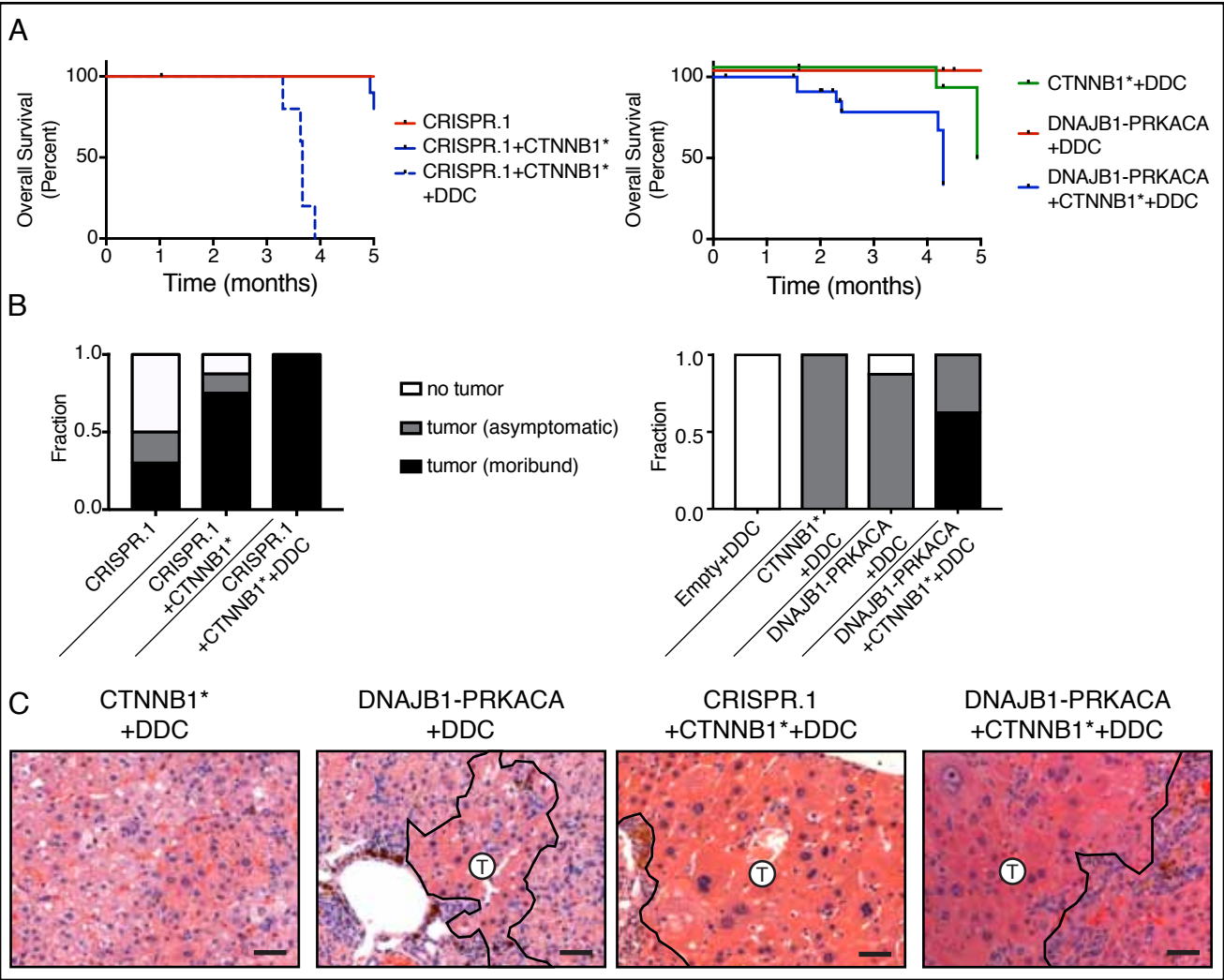

Figure 7. Tumorigenicity of DNAJB1-PRKACA is dependent on kinase domain.

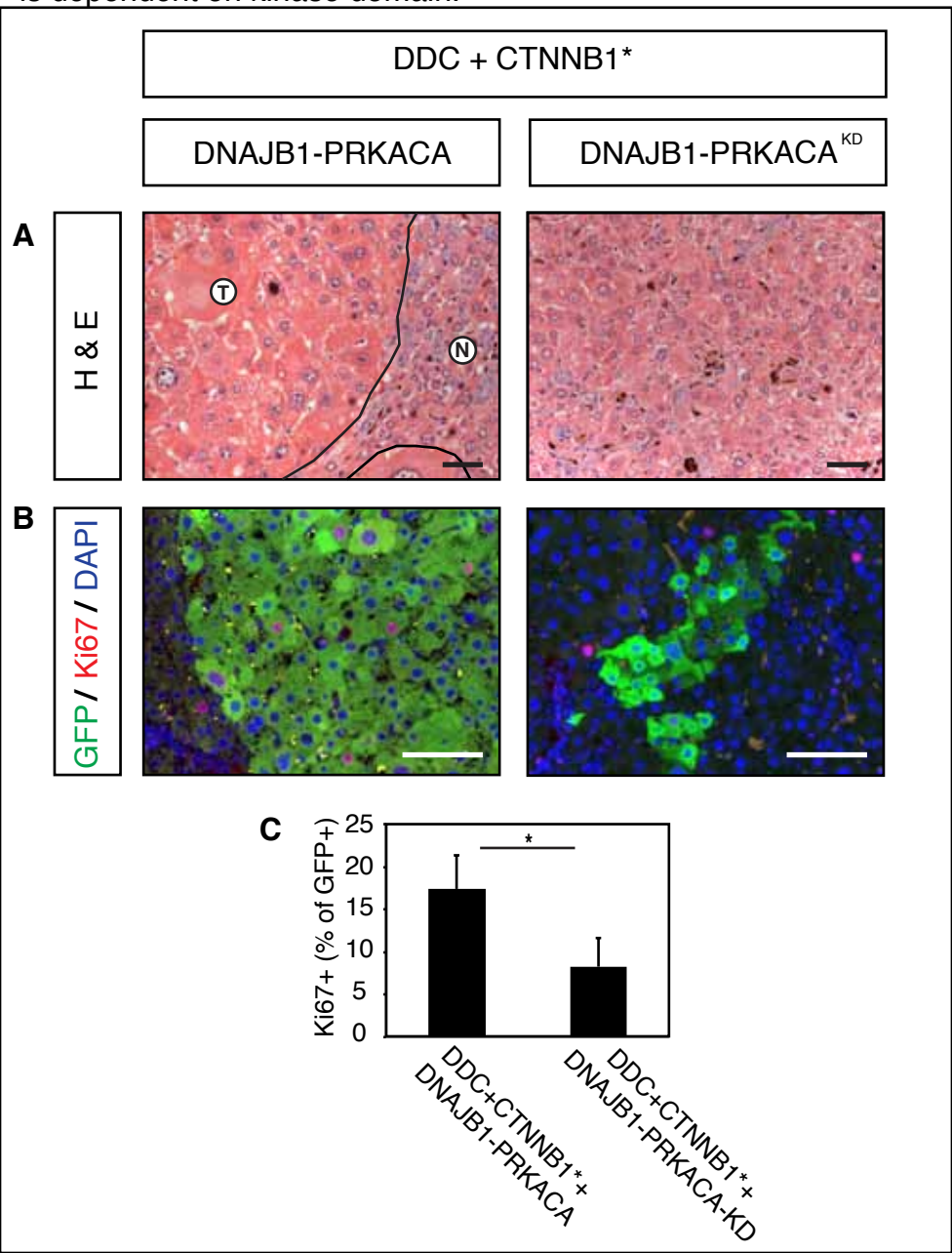

Supplementary Figure 1. Validation of CRISPR-mediated deletion

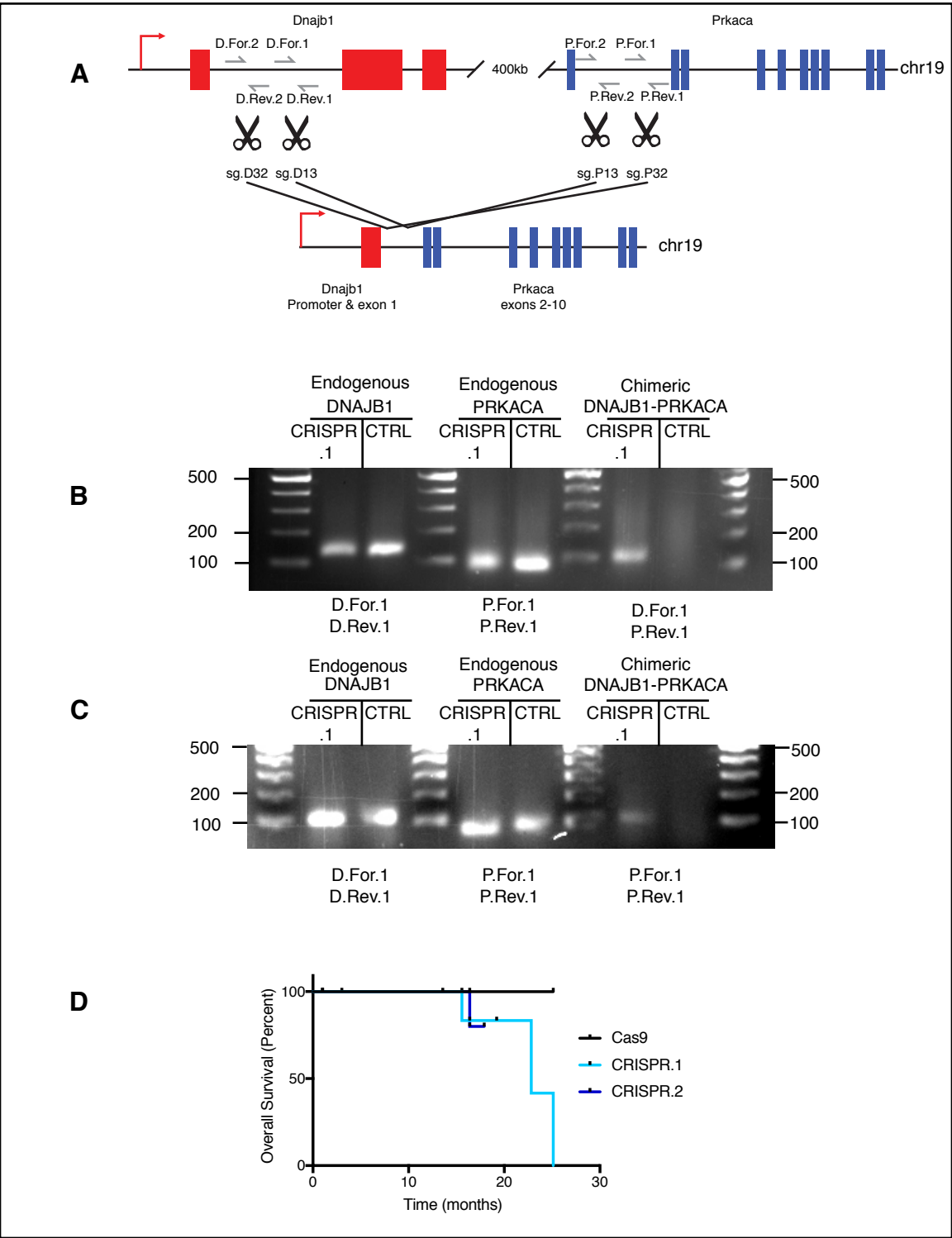

Supplementary Figure 2. Additional ultrastructural analysis of murine FL-HCC.

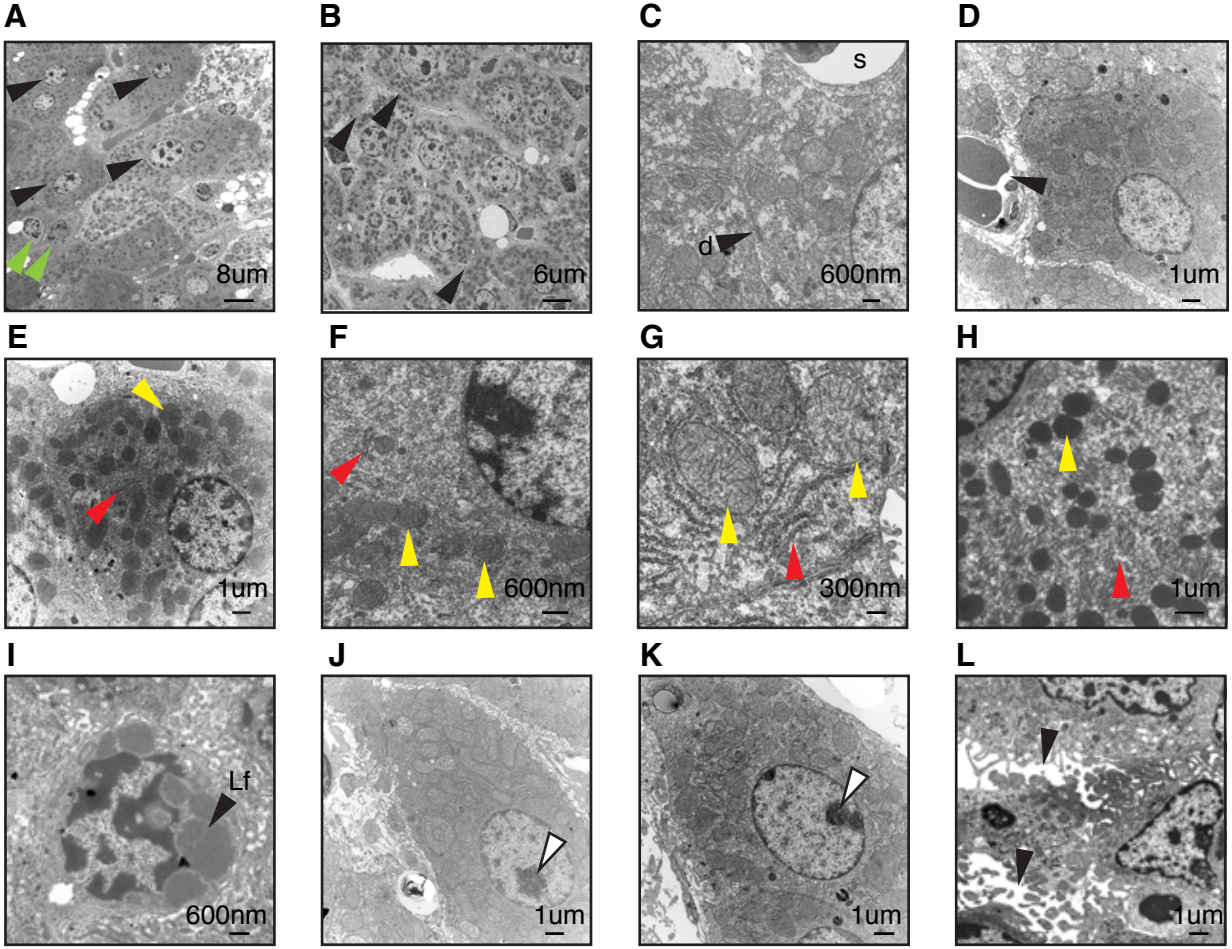

Supplementary Figure 3. Additional molecular characterization of murine FL-HCC.

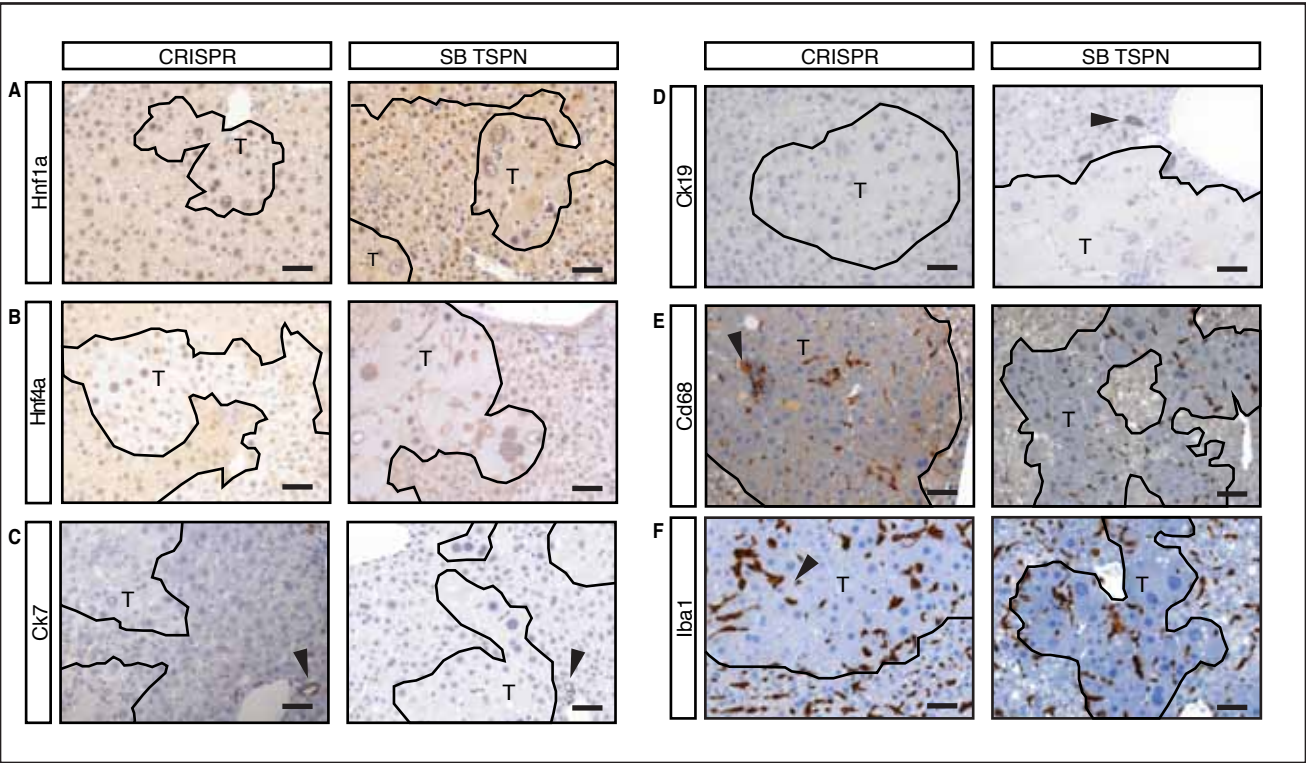

Supplementary Figure 4. Copy Number profiling of murine FL-HCC

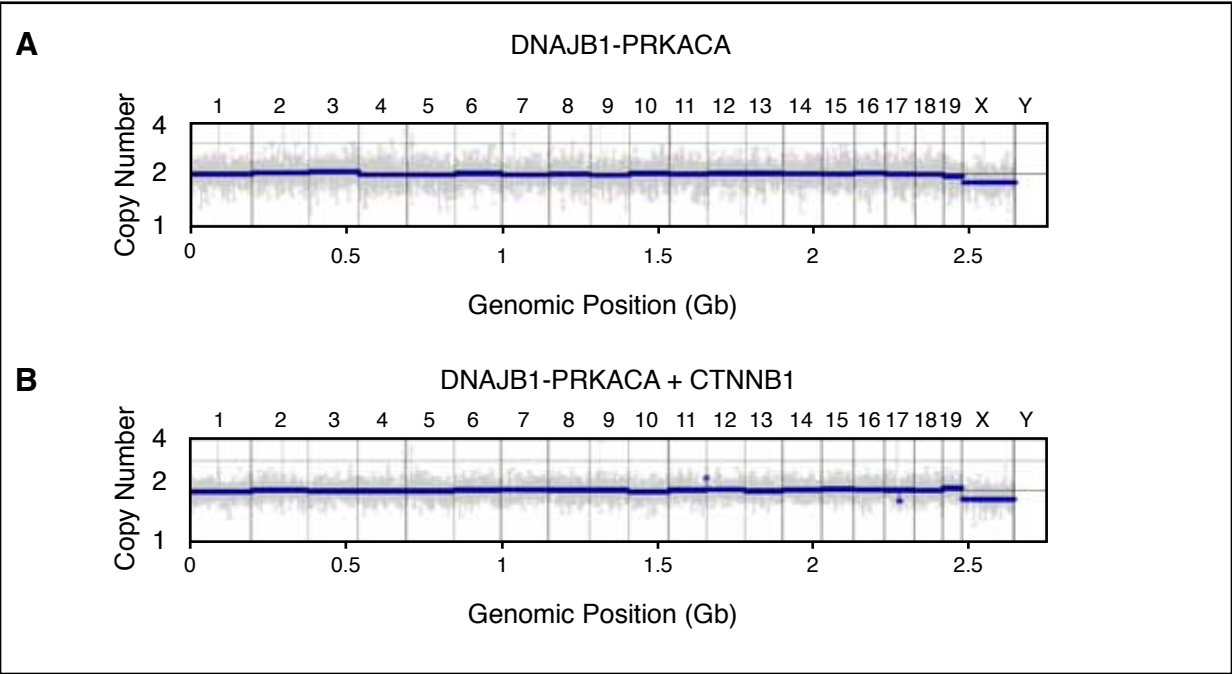

Supplementary Figure 5. Gene expression of FL-HCC-associated genesets of interest.

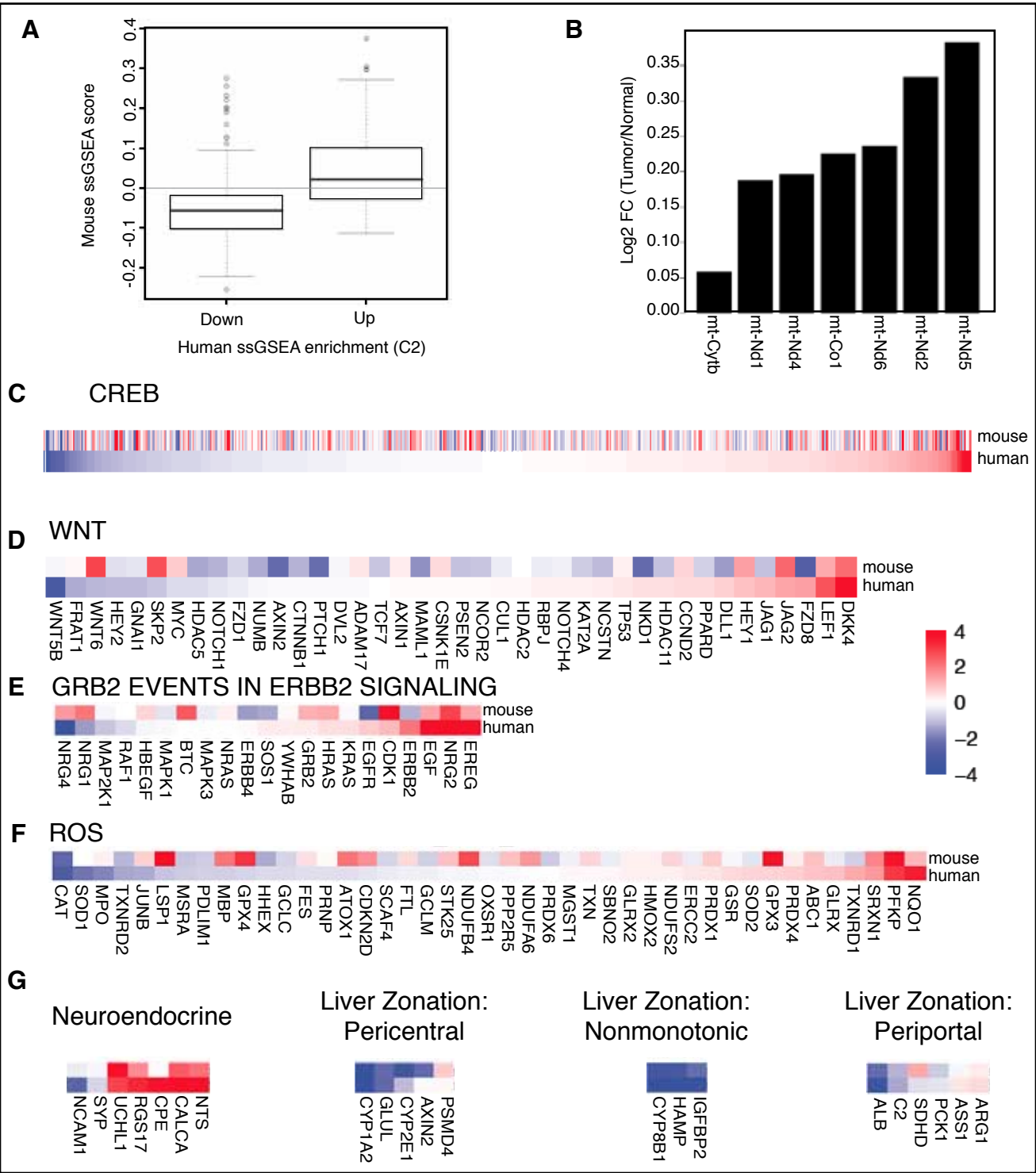

Supplementary Figure 6. WNT pathway in human FL-HCC.

a

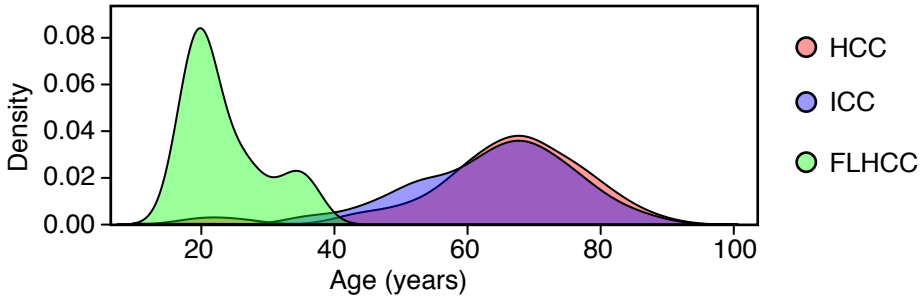

b

Age	Gender	Mutations	CNA	Survival Status	Survival (months)
18	Male	DNAJB1-PRKACA, APC, CHEK2	TERT^{AMP}	Alive	29
18	Male	DNAJB1-PRKACA, CTNNB1	none	Alive	15
21	Female	DNAJB1-PRKACA, CTNNB1 LOC101928035-ZFHX3, ATR (met only)	SOX17^{AMP} (Met only)	Alive, Brain Metastasis	31

c

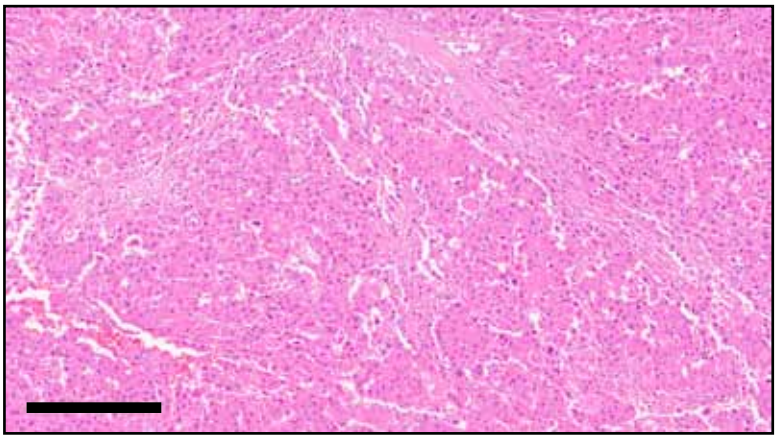

Supplementary Figure 7. WNT pathway in mouse FL-HCC.

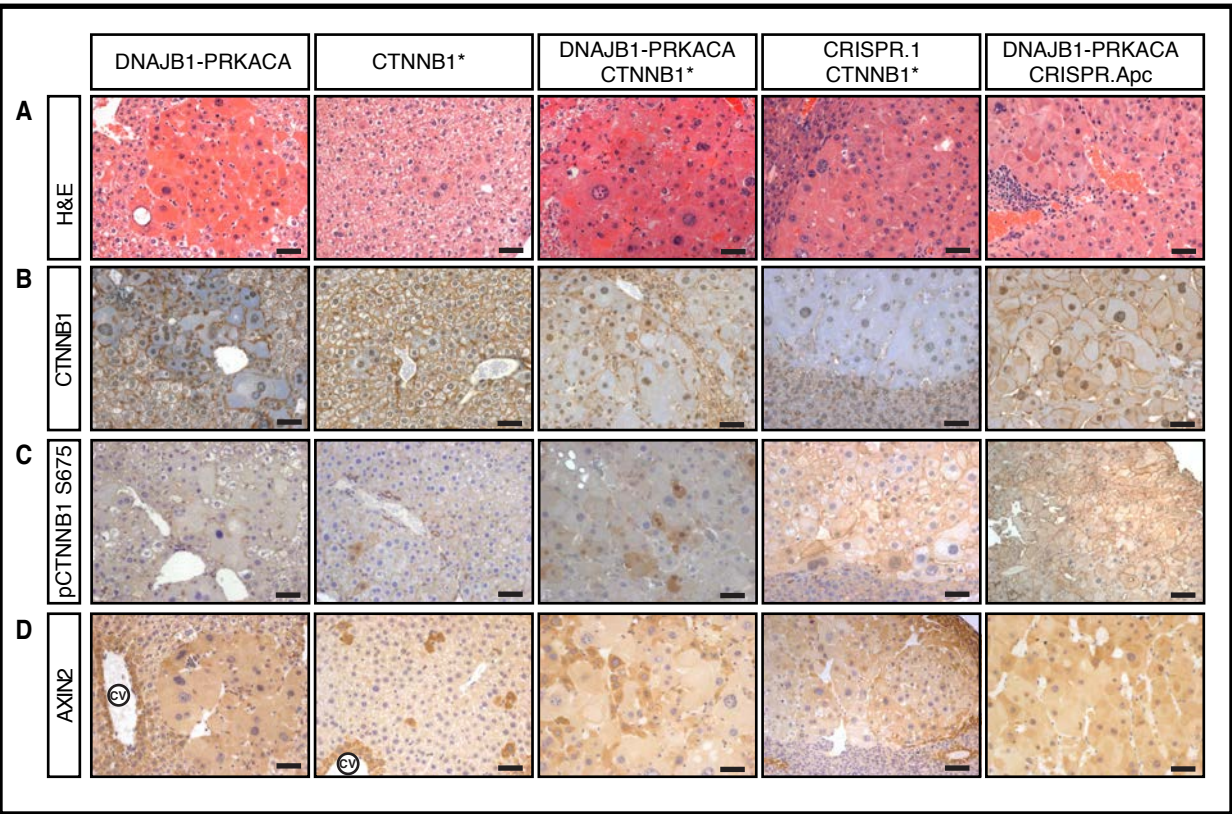
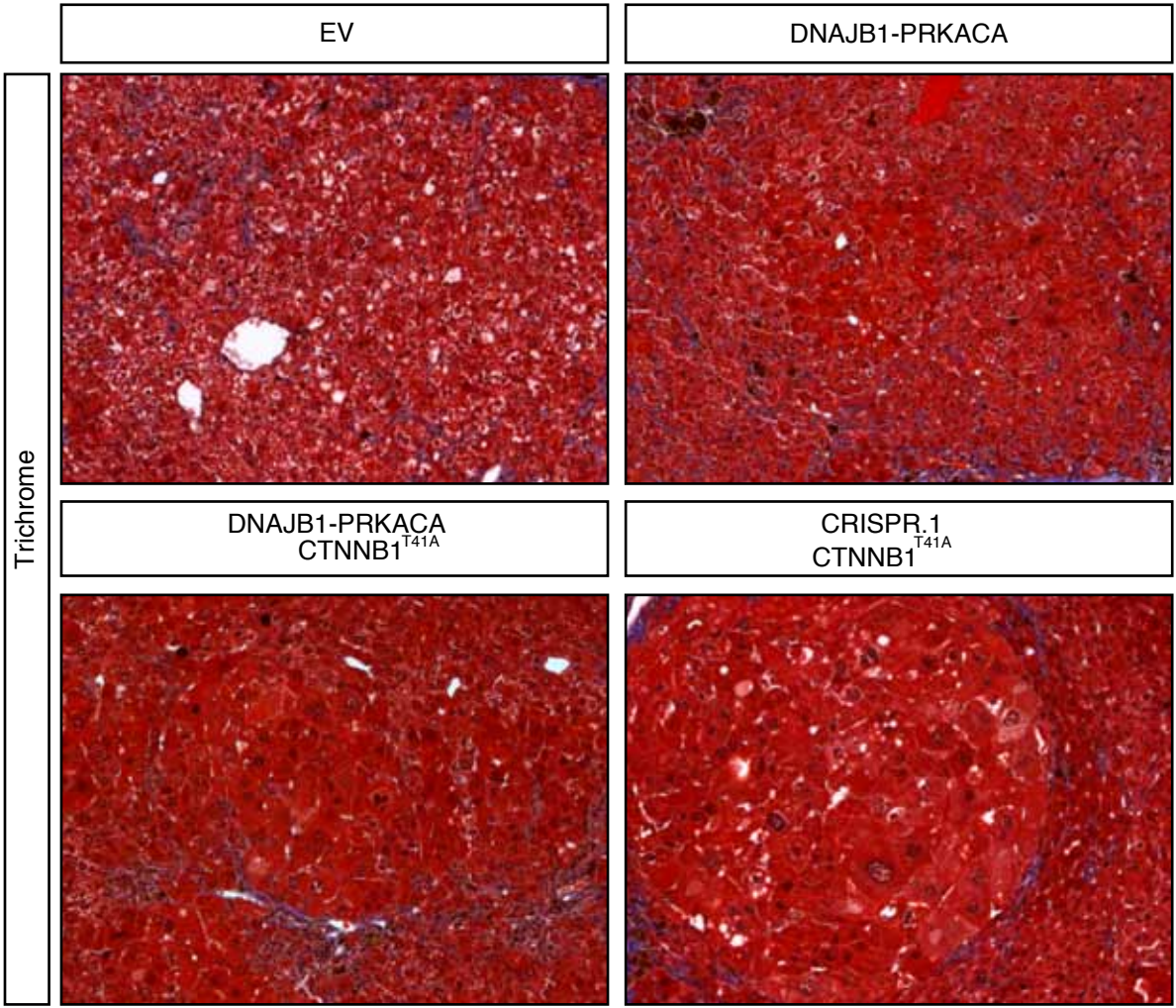
Supplementary Figure 8. Fibrosis following DDC.